INVESTIGATION OF PARALLEL PLANAR DEFECTS AND TEXTURE TRANSFORMATION IN ELECTRON BEAM EVAPORATED SILVER THIN FILMS

A Thesis

Presented to the Faculty of the Graduate School

of Cornell University

in Partial Fulfillment of the Requirements for the Degree of

Master of Science

by

Shelby Leigh Johnson

August 2015

ABSTRACT

Texture transformation is a known phenomenon which occurs in face-centered cubic metal thin films. This phenomenon entails a transition of film texture from (111) in as-deposited films to (100) in post-annealed films depending on film thickness; thinner films maintain the as-deposited (111) texture while thicker films transform to (100) texture after heat treatment. Texture transformation was previously theorized to result from minimization of surface and interface energies and strain energy; however, additional evidence contradicts this theory, suggesting that an alternative driving force for texture transformation exists. Nanotwin defects have been observed in numerous face-centered cubic metal thin films and may be a driving force for texture transformation; whether or not film nanotwin density is affected by changes in deposition parameters is not yet agreed upon. The influence of deposition rate on nanotwin density and texture transformation of silver thin films is investigated in this work. Silver thin films were synthesized at varied deposition rates using electron beam evaporation. Film samples were annealed to induce texture transformation using two setups; the first setup was used to analyze texture transformation of samples with different thicknesses deposited at different rates and the second setup was used to analyze texture transformation of samples with identical thickness deposited at different rates in situ over time. The texture of thin film samples was analyzed using x-ray diffraction. To identify and characterize nanotwins in our thin films cross-sections of film samples were studied using transmission electron microscopy.

X-ray diffraction measurements indicated that the as-deposited silver thin films had strong (111) texture and that thicker films developed partial or transformed completely to (100) texture after heat treatment. Investigation of x-ray diffraction measurements of samples deposited at different rates revealed that changes in deposition rate influence texture transformation in thin film samples. Increasing deposition rate was found to increase texture transformation in film samples; samples of identical thickness deposited at faster rates were found to have a higher (100) texture post anneal than samples deposited at slower rates and from the in situ study samples of identical thickness deposited at faster rates were found to have

transformed in less time than samples deposited at slower rates. Transmission electron microscopy results for as-deposited silver film samples showed that nanotwins were in our evaporated silver thin films parallel to the substrate. Investigation of samples deposited at different rates revealed that changes in deposition rate influence nanotwin spacing in film samples. Increasing deposition rate was found to decrease nanotwin spacing in silver thin film samples.

Nanotwins are found to be a viable driving force for texture transformation in face-centered cubic metal thin films in this work. A model based on classical nucleation theory modified for formation of twinned and untwined nuclei from a vapor phase was assessed as a method for predicting nanotwin spacing in thin films. Results from applying this model were found to closely match experimental nanotwin spacing measurements in our silver thin films samples; however, the use of this model is still questionable.

BIOGRAPHICAL SKETCH

Shelby is from Rockville, Maryland. She received her Bachelor of Science degree in Integrated Natural Science and Engineering at Lehigh University where she studied Chemistry and Materials Science and Engineering. Shelby came to Cornell University to pursue her interest in Materials Science and Engineering and has greatly enjoyed having the opportunity to meet and work with such amazing individuals during her time as a graduate student.

ACKNOWLEDGEMENTS

I would like to express my appreciation to Professor Brandon Hoffman, Kyle Flemington, Paul Lashomb, and Jonathon Yuly from Houghton College for all of their help with sample annealing experiments and x-ray diffraction measurements for this project.

I would also like to thank Elizabeth A. Ellis for her work on this project, including film deposition, profilometry and TEM and for her guidance during my time at Cornell. I would also like to thank Elizabeth and Markus Chmielus for depositing and performing x-ray diffraction measurements on a silver thin film sample.

I would like to thank Nathaniel G. Rogers for all of his help throughout this project including film deposition, sample annealing and x-ray diffraction measurements.

I would like to express my gratitude to Rekha King and Ari Kestenbaum for their assistance with sample deposition.

Finally, I would like to thank my advisor, Professor Shefford P. Baker, for all of his guidance during my time at Cornell.

This work was supported by the National Science Foundation (NSF) via grant Nr. DMR-1106223 and DMR-1411024, including a Research Experiences for Undergraduates supplement. This work made use of the Cornell Center for Materials Research Shared Facilities which are supported through the NSF MRSEC program (DMR-1120296). Brandon Hoffman, Kyle Flemington, Paul Lashomb and Jonathan Yuly received additional financial support from Houghton College.

TABLE OF CONTENTS

LIST OF FIGURES

LIST OF TABLES

CHAPTER ONE

INTRODUCTION

A unique phenomenon has been observed in face-centered cubic (FCC) metal thin films in which the texture of a film transitions from the as-deposited texture of primarily (111) oriented grains to a texture of predominantly (100) oriented grains when film samples are annealed [1–14]. Understanding this phenomenon is important for materials design as the microstructure and the material properties, including mechanical properties, of a thin film are directly related, and thus the functionality and reliability of a film are affected by this transition in texture [15,16].

Polycrystalline thin films are composed of many grains and each grain has a specific crystallographic orientation. When the orientations of these grains are not random, the grains have a "preferred orientation" and the film has a specific "texture" [17,18]. When the microstructure of a film is made up of grains with an identical (hkl) plane parallel to the substrate, but the orientation of other planes perpendicular to the substrate have a random orientation distribution, the film has a specific fiber texture [19]. Since FCC metals are anisotropic, material properties are dependent on crystallographic orientation [20,21], thus physical and mechanical properties are determined by the film texture [17].

The focus of this project is the study of texture transformation in electron beam evaporated silver thin films. The fiber texture of the silver films changes when the films are subjected to heat treatments. If the texture of the film is altered, then it follows that the material properties of the film are also changed. Understanding the driving force for texture transformation is essential to controlling film microstructure and optimizing film properties for specific applications.

1.1 Texture Transformation

Texture transformation is an interesting phenomenon that has been observed in FCC metal thin films that entails a transition of the out of plane crystallographic orientation of grains in the growth direction from primarily (111) in as-deposited films to predominantly (100) in post-annealed films [1–14], depending on film thickness [2,4–14].

Texture transformation has been previously theorized to result from the minimization of strain and interface energies [4–8]. Due to the anisotropy of FCC metals, material properties are orientation dependent; the (111) orientation minimizes interface energy [2,4–8] while the (100) orientation minimizes strain energy [1,2,4–8] because the (111) orientation tends to have a lower surface and interface energies while (100) the orientation tends to have a lower biaxial modulus than other orientations in FCC metals [8,13,14]. Assuming a complete transition from a film that has entirely (111) texture to a film with entirely (100) texture the change in strain energy and the change in surface energy for the texture transformation are represented by Equation 1.1 [14] and Equation 1.2 respectively [8].

$$\Delta\phi_{\varepsilon} = (\sigma_{100} - \sigma_{111}) \cdot h\varepsilon \tag{1.1}$$

$$\Delta\phi_{\gamma} = (\gamma_{s,100} - \gamma_{s,111}) + (\gamma_{i,100} - \gamma_{i,111}) \tag{1.2}$$

In Equation 1.1 σ_{100} and σ_{111} are the stresses, h is film thickness and ε is strain in the film samples [14]. In Equation (2) $\gamma_{s,100}$ and $\gamma_{s,111}$ are silver surface energies for (100) and (111) orientations respectively and $\gamma_{i,100}$ and $\gamma_{i,111}$ are Ag/Ti interface energies for (100) and (111) orientations [8]. As values for Ag/Ti interface energies for different orientations of Ag are not known, surface energy is approximated by Equation 1.3 [14] which treats the Ag/Ti interface as a silver surface.

$$\Delta\phi_{\gamma} = 2 \cdot (\gamma_{100} - \gamma_{111}) \tag{1.3}$$

In Equations 1.3 γ_{100} and γ_{111} are surface energies for silver for (100) and (111) orientations [14]. According to this theory, it follows that some critical thickness exists below which films retain

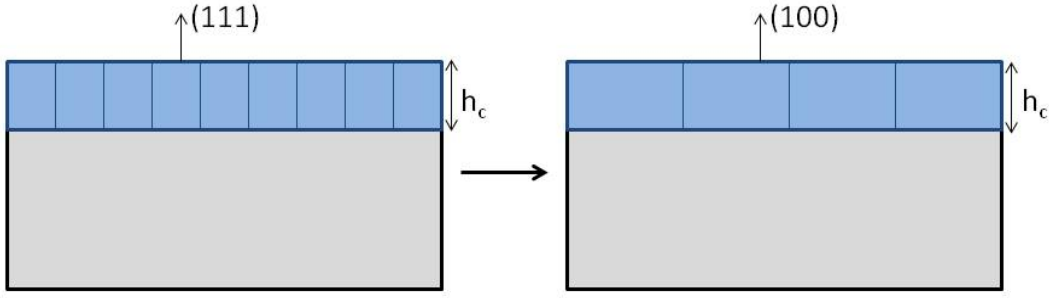

Figure 1.1: Sketch demonstrating critical film thickness, h_c, below which film retains as-deposited (111) texture and above which texture transforms from as-deposited (111) texture to (100) texture with heat treatment.

their (111) as-deposited texture and above which films transform to have a (100) texture [7,8,13]; this is demonstrated in Figure 1.1. Following the assumption of a complete transformation from 100% (111) to 100% (100) the critical thickness is represented by Equation 1.4.

$$h_c = \frac{2}{\sigma_{111}^2}\left(\gamma_{100} - \gamma_{111}\right)\left(\frac{Y_{111}^2}{Y_{111} - Y_{100}}\right) \tag{1.4}$$

In Equation 1.4 h_c is the critical thickness, σ_{111} the stress in the as-deposited film, and Y_{111} and Y_{100} are the respective biaxial moduli for (111) and (100) [13]. In thinner films, surface energy minimization is dominant and in thicker films strain energy minimization is dominant.

Evidence from other studies is indicative of the existence of an alternative driving force to account for observed texture transformation [9,10,12–14]. Baker *et al.* [14] deposited silver thin film samples via evaporation and measured stresses in the silver film samples in situ during heating. Baker *et al*. [14] observed texture transformation in thicker samples but found that the measured stresses in the film samples were not high enough to induce the texture transformation that occurred. Because the stresses in the film were not high enough to cause texture transformation, the film samples should have retained their as-deposited texture in accordance with the strain energy and interface/surface energy minimization theory.

In addition, Greiser *et al.* [9,10] reported texture transformation in sputter deposited silver thin films that had been removed from their substrate and annealed as free-standing films. These results are unexpected because the earlier theory of minimization of strain and surface/interface energies indicated that free-standing films would maintain their as-deposited texture since the source of strain had been removed.

From the experimental results of the aforementioned studies it has been ascertained that the early theory describing texture transformation in terms of strain energy and surface/interface energy minimization is incomplete. An additional driving force that accounts for the observed behavior must exist.

1.2 Defects in Thin Films

Defects are known to exist in thin films [22]. There are three different categories of defects: point defects such as vacancies, line defects like dislocations and planar defects including stacking faults and twins. Excess energy is associated with defects due to an associated formation energy required to form defects. The excess energy is released as defects are annihilated [23]. If defects are annihilated during heat treatment of thin films, then the excess energy associated with those defects may drive texture transformation.

Sonnweber-Ribic *et al*. [12] used magnetron sputtering to deposit copper films and calculated the driving forces for strain energy and interface/surface energy minimization based on their deposition parameters. Sonnweber-Ribic *et al*. [12] found from the results of their calculations that texture transformation should not occur in their copper thin film samples because the strain energy driving force never exceeded the surface energy driving force, meaning that transformation to (100) texture was never energetically favorable. The discrepancy between their calculations and experimental observations led Sonnweber-Ribic *et al.* [12] to speculate that the elimination of dislocations was a probable additional driving force for texture transformation. Sonweber-Ribic *et al.* [12] found that (100) grains have a greater dislocation density than (111) grains and so the (100) have a faster recovery during annealing. However, an explanation that addresses why (100) grains would have a greater dislocation density than (111) grains is not given.

Film defect density may be a driving force for texture transformation if defects are annihilated during annealing. Sonnweber-Ribic *et al.* [12] speculated that dislocations affect texture transformation, but their argument does not address the orientation dependent grain growth observed in texture transformation. Another type of defect must contribute to texture transformation.

1.3 Parallel Planar Defects

Parallel planar defects are planar defects including stacking faults and growth twins that are oriented parallel to the substrate. Growth twins, or nanotwins, have been experimentally

observed in FCC metal thin films including copper and copper alloys [3,24–30], silver [31,32], palladium [33,34], nickel [24] and 330 stainless steel [35]. These different metal thin films are synthesized using a variety of methods; most films are deposited via sputtering [3,24,26–28,30–32,35], another less common method is evaporation [33,34], and another method is electrodeposition [25,29], which will not be focused on in this work. Recent interest in these nanotwins has developed because of their potential for strengthening thin films; nanotwins have been found to strengthen FCC metal thin films [25,26,32].

Nanotwins develop in (111) oriented grains as a result of the stacking sequence of atoms in the (111) crystallographic orientation in FCC structures. In the (111) orientation of an FCC lattice structure, atoms follow an ABCABC stacking sequence, and so incoming adatoms are able to occupy either a parent or a twin lattice site on the (111) oriented grains [1,36,37]; this is demonstrated in Figure 1.2. In Figure 1.2 (A), the stacking sequence is ABC, showing a perfect stacking sequence, while in Figure 1.2 (B) the stacking sequence is ABA showing a twin stacking sequence.

As proposed in the previous section, if nanotwins are eliminated during annealing and subsequence grain growth then the energy from eliminating those defects may be a driving force for texture transformation. An illustration of the growth process of either (111) or (100) grains during annealing is shown in Figure 1.3. In Figure 1.3 (A) an as-deposited film sample is shown with a (111) grain that contains nanotwins parallel to the substrate next to a (100) grain

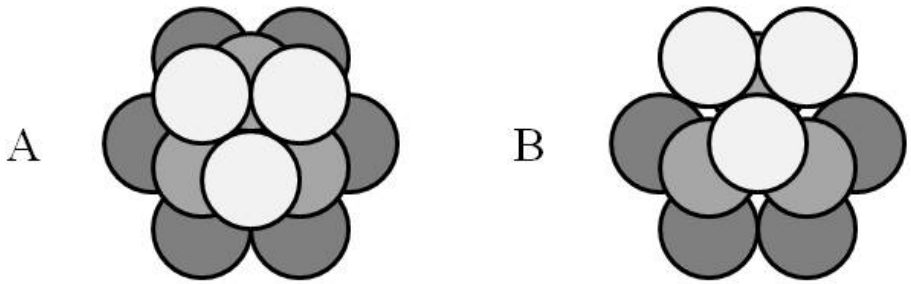

Figure 1.2: Cartoon demonstrating top view of packing sequence for (111) orientation in FCC material; (A) depicts formation of perfect lattice and ABC stacking while (B) shows formation of nanotwin and ABA stacking

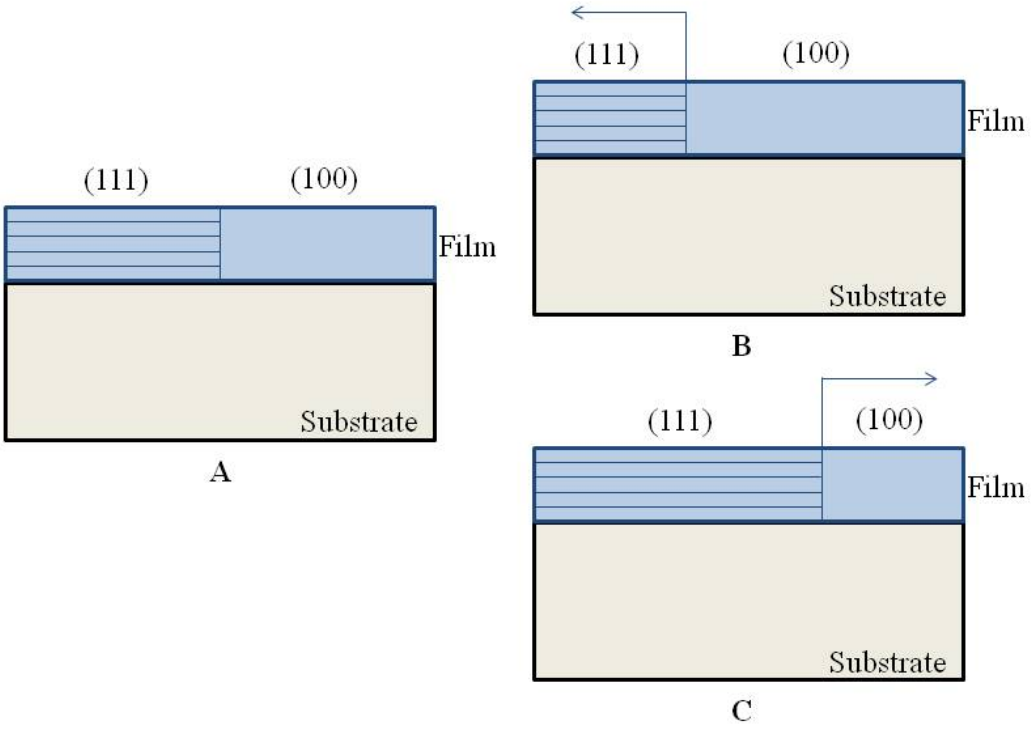

Figure 1.3: Illustration of grain growth during annealing with (A) showing an as-deposited film microstructure, (B) showing growth of a (100) oriented grain containing no nanotwins and (C) showing growth of a (111) grain containing nanotwins

containing no nanotwins. Figure 1.3 (B) and (C) respectively show the growth of the (100) grain at the expense of the (111) grain and the growth of the (111) grain at the expense of the (100) grain. As shown by Figure 1.3 (B) growth of (100) grains at the expense of (111) grains is energetically favorable because as (100) grains grow nanotwins in (111) grains are eliminated, whereas in Figure 1.3 (C) growth of (111) grains requires the propagation of those parallel nanotwins, which is an energy intensive process. Because texture transformation in FCC metal thin films is known to entail growth of (100) grains at the expense of (111) grains [1–14] the mechanism of eliminating nanotwins fits as a potential driving force for texture transformation. If nanotwins exist in the silver thin film samples investigated in this work and if they are eliminated during heat treatment then nanotwins may drive texture transformation.

1.4 Deposition Parameters and Nanotwin Formation

A potential relationship between deposition parameters such as deposition rate and substrate temperature and nanotwin formation in FCC metal thin films has been explored. Zhou and Wadley [36] performed molecular dynamic (MD) simulations to model vapor deposition of copper thin films and also used phase field analysis of copper vapor deposition to closely study the development of nanotwins in copper films. From their simulation results Zhou and Wadley [36] determined that deposition rate and substrate temperature would not significantly influence nanotwin growth during deposition.

In another study, Zhang *et al.* [38] observed nanotwins in their sputter deposited multilayer thin films of copper and 330 stainless steel and then applied a model based on classical nucleation theory, modified by Han *et al.* [37] for formation of twinned and untwined nuclei, and altered for nucleation from a vapor phase to explain the microstructure of their multilayer films. Zhang *et al.* [38] determined that increasing the rate at which a film is deposited increases the likelihood of forming nanotwins in thin films.

Based on conflicting evidence presented by Zhou and Wadley [36] and Zhang *et al.* [38] whether or not deposition parameters affect nanotwin formation in FCC thin films remains unclear. If deposition parameters do influence nanotwin formation in FCC thin films then nanotwin density can be controlled.

1.5 Thesis Overview

Nanotwins have been observed in multiple FCC metal thin films, but a link between defect density and texture transformation has not yet been established. Also, the mechanism by which nanotwins develop in thin films during deposition and the potential influence of deposition parameters on nanotwin formation are not well understood. To address these challenges we have designed experiments and utilized numerous analytical techniques that would demonstrate a connection among deposition parameters, nanotwin defect density, and texture transformation in electron beam evaporated silver thin films.

Thin films were deposited such that samples with different thicknesses were exposed to identical deposition conditions. The deposition rate used to synthesize the silver films was varied among the films to determine if and how the rate at which the films were deposited influenced film microstructure. The substrate temperature was monitored to measure the substrate temperature during deposition. After deposition, film samples were annealed to induce texture transformation. These experimental setups are further discussed in Chapters 2, 3 and 4.

The as-deposited and post-anneal film texture was approximated by using x-ray diffraction to establish (111) and (100) fractional intensities. Transmission electron microscopy was utilized to analyze cross-sections of silver film samples and determine if parallel planar defects were present in the samples and how the defect density varied among the samples. The results of these analyses are presented in Chapters 3 and 4.

Chapter 2 of this thesis reviews experimental setup and analytical techniques utilized for this project in greater detail. Chapter 3 of this thesis serves to establish a relationship between parallel planar defect density and texture transformation in silver thin film samples. In Chapter 4 a relationship between parallel planar defect density and deposition parameters is established and a theory for nucleation is reviewed for modeling nanotwin development in thin films. Finally, in Chapter 5 are conclusions from this project along with recommendations for future work.

REFERENCES

[1] Vook RW, Witt F. J Vac Sci Technol 1965;2:49.

[2] Vook RW, Witt F. J Vac Sci Technol 1965;2:243.

[3] Dahlgren SD. J Vac Sci Technol 1974;11:832.

[4] Zielinski EM, Vinci RP, Bravman JC. J Appl Phys 1994;76:4516.

[5] Floro JA, Thompson C V, Carel R, Bristowe PD. J Mater Res 1994;9:2411.

[6] Thompson CV, Carel R. Mater Sci Eng B 1995;32:211.

[7] Carel R, Thompson CV, Frost HJ. Acta Mater 1996;44:2479.

[8] Thompson CV, Carel R. Mater Sci Forum 1996;204-206:83.

[9] Greiser J, Muller D, Mullner P, Thompson C V, Arzt E. Scr Mater 1999;41:709.

[10] Greiser J, Mullner P, Arzt E. Acta Mater 2001;49:1041.

[11] Sonnweber-Ribic P, Gruber P, Dehm G, Arzt E. Acta Mater 2006;54:3863.

[12] Sonnweber-Ribic P, Gruber PA, Dehm G, Strunk HP, Arzt E. Acta Mater 2012;60:2397.

[13] Baker SP, Hoffman B, Timian L, Silvernail A, Ellis E a. Acta Mater 2013;61:7121.

[14] Baker SP, Saha K, Shu JB. Appl Phys Lett 2013;103:191905.

[15] Vinci RP, Zielinski EM, Bravman JC. Thin Solid Films 1995;262:142.

[16] Knorr DB. Mat Res Soc Symp Proc 1993;309:75.

[17] Ohring M. Materials Science of Thin Films: Deposition and Structure, Second. Academic Press; 2002.

[18] Cullity BD, Stock SR. Elements of X-Ray Diffraction, Third. Prentice Hall; 2001.

[19] Brundle CR, Evans Jr. CA, Wilson S. Encyclopedia of Materials Characterization. Greenwich, CT, U.S.A.: Manning Publications Co.; 1992.

[20] Boas W, Mackenzie JK. Prog Met Phys 1950;2:90.

[21] Kocks UF, Tome CN, Wenk H-R. Texture and Anisotropy. Cambridge University Press; 1998.

[22] Neugebauer CA. Condensation, Nucleation, and Growth of Thin Films, in:. Maissel LI, Glang R (Eds.). Handb. Thin Film Technol. New York, NY, U.S.A.: McGraw-Hill, Inc.; 1970.

[23] Laughlin DE, Hono K, editors. Physical Metallurgy Volume I, fifth ed. Waltham, MA, U.S.A.: Elsevier B.V.; 2014.

[24] Wang R, Dahlgren SD. J Mater Sci 1975;10:1456.

[25] Lu L, Shen Y, Chen X, Qian L, Lu K. Science (80-) 2004;304:422.

[26] Zhang X, Wang H, Chen XH, Lu L, Lu K, Hoagland RG, Misra A. Appl Phys Lett 2006;88.

[27] Hodge AM, Wang YM, Barbee Jr. TW. Mater Sci Eng A 2006;429:272.

[28] Anderoglu O, Misra a., Wang H, Zhang X. J Appl Phys 2008;103:094322.

[29] Liu T-C, Liu C-M, Hsiao H-Y, Lu J-L, Huang Y-S, Chen C. Cryst Growth Des 2012;12:5012.

[30] Velasco L, Polyakov MN, Hodge AM. Scr Mater 2014;83:33.

[31] Bufford D, Wang H, Zhang X. Acta Mater 2011;59:93.

[32] Furnish TA, Hodge AM. APL Mater 2014;2:046112.

[33] Wang B, Idrissi H, Shi H, Colla MS, Michotte S, Raskin JP, Pardoen T, Schryvers D. Scr Mater 2012;66:866.

[34] Amin-Ahmadi B, Idrissi H, Galceran M, Colla MS, Raskin JP, Pardoen T, Godet S, Schryvers D. Thin Solid Films 2013;539:145.

[35] Zhang X, Misra a., Wang H, Nastasi M, Embury JD, Mitchell TE, Hoagland RG, Hirth JP. Appl Phys Lett 2004;84:1096.

[36] Zhou XW, Wadley HNG. Acta Mater 1999;47:1063.

[37] Han K, Hirth JP, Embury JD. Acta Mater 2001;49:1537.

[38] Zhang X, Misra A, Wang H, Shen TD, Nastasi M, Mitchell TE, Hirth JP, Hoagland RG, Embury JD. Acta Mater 2004;52:995.

CHAPTER TWO

METHODS

The focus of this work is the investigation of silver thin films that are synthesized via electron beam (e-beam) evaporation, a type of physical vapor deposition. Physical vapor deposition is one category of thin film formation in which a source material is vaporized by means of heat or an energetic beam of positive ions, photons, or electrons to produce a film on a substrate [1]. Most previous studies of texture transformation [2–7] or nanotwins [2,8–16] in FCC thin films have been of samples deposited via sputtering. A second type of physical vapor deposition, and so an overview of both types of physical vapor deposition is given.

2.1 Electron Beam Evaporation and Sputter Deposition

Electron beam (e-beam) evaporation is an economical method for producing metal films [17] that entails depositing films atomistically under vacuum by means of a controlled transport of atoms from a source, heated by an electron beam heating element, to a substrate by transferring thermal energy [18] as shown in Figure 2.1. An electron beam is curved by a magnetic field such that it comes in contact with source material at the center of a crucible sitting in a hearth [18]. The source material is heated by the electron beam, melts and then evaporates, and metal atoms travel from the crucible to a substrate placed directly above the crucible. E-beam evaporation is a preferred method of deposition because a variety of metal sources can be evaporated and the resulting thin films have high purity [18]. High sample purity is achievable because the metal to be deposited is contained in a crucible that is water-cooled, ensuring that only the surface reaches a high temperature and therefore any reactions between the crucible and metal that could lead to contamination of the final film are eliminated [18–20]. E-beam evaporation is also advantageous because the heating source has a high power density and as a result a large range of evaporation rates, from very fast to very slow, is achievable [20]. E-beam evaporation is desirable for depositing thin films at fast deposition rates [19].

A second physical vapor deposition method that is widely utilized is sputtering. Many examples of experimentally observed nanotwins have been found in sputter deposited thin film

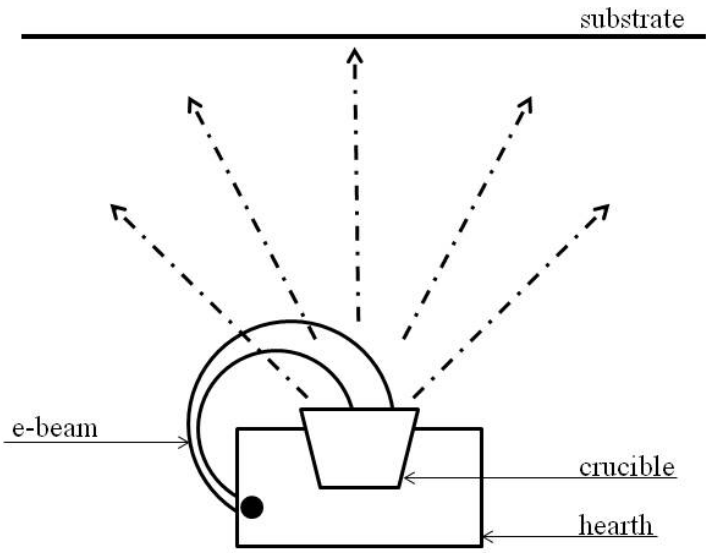

Figure 2.1: Depiction of e-beam evaporation process demonstrating how the e-beam is curved by a magnetic field onto metal in a crucible to evaporate the metal adatoms onto the substrate above source material [18].

samples [2,9,13–15]. Sputtering has many variations, but generally consists of positive ions striking a target and then neutral atoms that are ejected from that target due to momentum transfer are condensed on a substrate forming a thin film [21]. A working gas, usually argon, is used in the chamber to serve as a medium through which the plasma is sustained [18]. Some benefits of the sputtering deposition process are excellent film uniformity, high deposition rates and thickness control [20].

2.2 Electron Beam Evaporation of Silver Thin Films

Silver thin film samples were deposited onto 100 mm diameter silicon substrates using electron beam evaporation. A schematic of the experimental setup within the vacuum chamber is shown in Figure 2.2. Within the vacuum chamber is a water cooled hearth into which crucibles, which hold a source material of metal pellets, are set. Directly above the hearth is a motorized rotatable stage with a substrate mount that holds a substrate during film deposition. Between the hearth and the substrate mount are two shutters used to shield a substrate from evaporating material. The sample shutter can be rotated to shield the substrate while source material is melted by an electron beam and during early stages of evaporation to limit sample contamination; the shutter

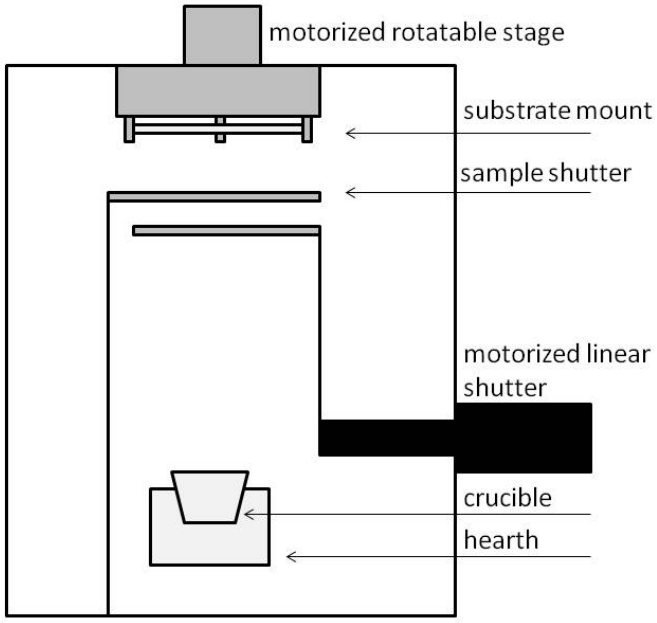

Figure 2.2: Sketch demonstrating experimental setup inside of vacuum chamber of evaporator for depositing film samples

can then be rotated to expose a substrate for film deposition. The motorized linear shutter can be programmed to cover or expose a substrate during deposition either gradually to create a thickness gradient film across a substrate or shield a portion of a substrate throughout deposition to deposit material on part of a substrate.

Silver and titanium pellets were cleaned using acetone, isopropanol, and deionized water. These cleaning steps were necessary to limit sample contamination during deposition. The silver pellets were loaded into a molybdenum crucible and the titanium pellets were loaded into a graphite crucible. Crucibles are filled less than 2/3 to prevent spillage of melted metal onto the hearth during deposition.

A rough pump and a cryogenic-pump were utilized to achieve the pressures necessary to produce successful samples. The rough pump was used to pump down the chamber to ~5 x 10^{-2} Torr, then the rough pump was shut down and the rough pump valve was closed to prevent oil contamination during the next stage of the vacuum setup. The rough pump is necessary to achieve the initial vacuum of ~5 x 10^{-2} Torr in the chamber so that the cryopump is

not overloaded during operation. Then a gate valve which separates the cryopump from the main chamber was opened to further pump down the chamber to ~2 x 10^{-6} Torr. Cryopumps are an ideal choice because a very high and clean vacuum is achievable using this type of pump [18].

A Thermionics 3 kW e-gun was used to evaporate the metal source materials. During deposition of film samples a current of ~0.1 amps was utilized for depositing a Ti adhesion layer and ~0.05-0.1 amps, depending on desired deposition rate, was used for depositing a silver layer. A thin titanium layer was deposited prior to each silver layer to promote adhesion of the silver film to the substrate and prevent the silver film from peeling off the substrate during annealing. An aluminum shield was placed across the diameter of each substrate to shield a portion of the substrate from source material for later profilometry measurements.

To obtain samples with varied thicknesses that were deposited under identical conditions a motorized linear shutter was programmed to cover the substrate as deposition progressed to create a thickness gradient, as shown in Figure 2.3. The rate at which the linear shutter was programmed to move depended on the desired gradient, deposition rate used, and length of the substrate wafer. To determine the time it would take to deposit the gradient Equation 2.1 was used.

$$t = \Delta h * \left(1 / R_{Ag}\right) \tag{2.1}$$

Where Δh is the desired thickness gradient in nanometers, R_{Ag} is the deposition rate of silver

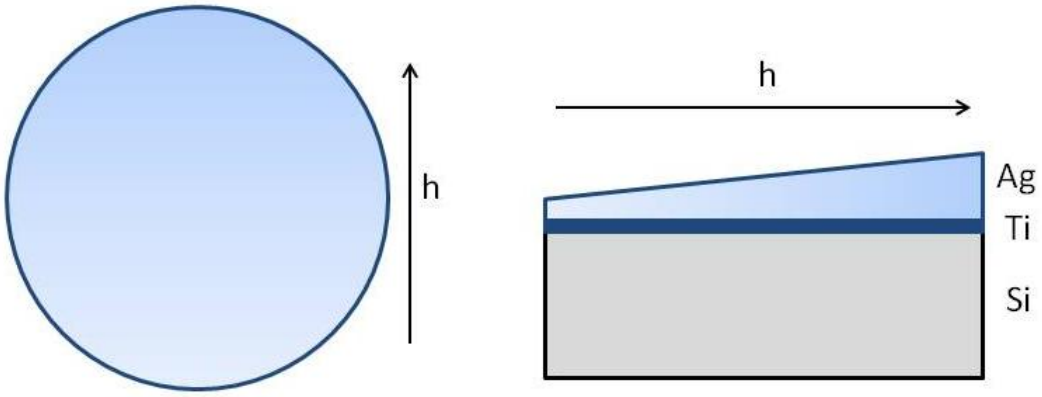

Figure 2.3: Illustration of film thickness gradient obtained using linear shutter

adatoms in nanometers per second, and *t* is the resultant deposition time in seconds. To determine the speed at which the linear shutter had to be programmed to move to achieve the desired gradient, Equation 2.2 was used.

$$v_{linearshutter} = l/t \tag{2.2}$$

Where *l* is the length of the silicon wafer in centimeters, *t* is the deposition time in seconds and $v_{linearshutter}$ is the resultant velocity of the linear shutter.

2.3 Sample Annealing Setups

Silver thin film samples were annealed using two different setups. The first annealing setup was used to investigate texture transformation in samples with varied thickness and deposition rates. Film samples were placed directly on a hotplate with the silver film facing up. A thermocouple was used to monitor the surface temperature of the hotplate and a sheet of aluminum foil was tented over the samples and hotplate to increase temperature uniformity. Silver film samples annealed via this method were heated at a temperature of 200 °C in air for two hours. Professor Brandon Hoffman and his students from Houghton College: Kyle Flemington, Paul Lashomb and Jonathon Yuly performed the annealing experiments for this first setup.

The second annealing setup was used to investigate texture transformation in silver film samples with similar thickness (~1800 nm) and varied deposition rates over time. A hot oil bath was assembled by pouring oil (Fischer Scientific, light mineral oil) into a Pyrex dish which was placed on a hotplate. A magnetic stir bar was added into the oil bath to promote temperature uniformity. An aluminum dish with an aluminum lid was placed in the oil bath such that the dish was partially submerged. A thermocouple was set up to monitor the surface temperature of the aluminum dish. Silver film samples were placed in the aluminum dish silver film side up. The silver samples were heated at a temperature of 100 °C in air over time. Samples were removed from the dish for periodic XRD measurements. Professor Brandon Hoffman and his students from Houghton College: Kyle Flemington, Paul Lashcomg and Jonathan Yuly performed two of three annealing experiments for this second setup.

2.4 Techniques for Sample Analysis

2.4.1 Profilometry

Profilometry is a mechanical method for measuring film thickness by sensing the movement of a stylus as it moves across a film-substrate step [18]. The film samples were marked every ~1 cm along the film center, where the aluminum shield had been located. Profilometry measurements were taken at the approximate center of each region using a contact profilometer (Tencor Alpha Step 500). To determine the thickness of the Ti adhesion layer, profilometry measurements were taken at the region of the film where only Ti had been deposited or measurements on the half of the film that had no Ti interlayer were utilized.

2.4.2 X-Ray Diffraction

Texture of thin films is usually obtained using XRD to measure pole figures [22–24]. This method entails maintaining a fixed 2θ diffraction angle while varying the tilt and rotation angles to obtain a pole figure [23,24]. One disadvantage with the pole figure method is that the technique is time intensive [25]. Film texture can be approximated more quickly by comparing peak intensities [25]. This technique is usable because only (111) and (100) peaks occur, (111) and (100) orientations are the only orientations that produce a signal with enough intensity for a peak to form in XRD spectrum, in XRD θ-2θ scans of the silver film samples analyzed in this work [26,27]. X-ray diffraction measurements were utilized to measure (111) and (100) fractional intensities of film samples which served as approximations for sample texture measurements. To estimate (111) and (100) fractional intensities both before and after heat treatment, the corrected area under intensity peaks from the x-ray diffraction spectrum were compared using Equations 2.3 and 2.4 [26,27].

$$f_{111} = I_{111}/(I_{111} + I_{100}) \tag{2.3}$$

$$f_{100} = I_{100}/(I_{100} + I_{111}) \tag{2.4}$$

Two XRD machines were utilized for these measurements (Scintag Theta-Theta X-ray Diffractometer and Rigaku SmartLab X-Ray Diffractometer), the operating parameters for which are specified in Table 2.1. Professor Brandon Hoffman, Kyle Flemington, Paul Lashomb and

Table 2.1: X-Ray diffraction operating parameters

	Scintag	Rigaku
X-Ray	40 kV 40 mA	40 kV 44 mA
Slit Size	2 mm	1 mm

Jonathon Yuly performed XRD scans for samples annealed using the first annealing setup and for two of three samples annealed using the second annealing setup.

An x-ray diffraction pattern is based on the orientation of the grains parallel to the substrate, so x-ray diffraction using theta/two-theta geometry is useful for determining texture and preferred orientation in polycrystalline thin films [25]. Peaks are compared to a powder diffraction file for silver to identify what grain orientation each peak represents. Long x-ray diffraction scans are obtained to determine what peaks are present, then local scans for the (111) and (100) peaks are obtained since those are the only peaks that occur in long scans. Local scans allow for better analysis of those (111) and (100) peaks and also take less time to obtain so for the second annealing setup the time that samples are away from the heating source for XRD analysis is minimized.

Peaks from XRD scans were analyzed using MDI Jade software. Area under each peak was obtained, corrected, and compared to determine fractional peak intensities. The values representing the area under a peak in the XRD scans are corrected to account for various factors which influence peak intensities [28]. An absorption factor is a correction for x-rays absorbed by the material which is represented by Equation 2.5 [28].

$$f_a = exp(-\mu x) \tag{2.5}$$

Where x is the path length, which is film thickness in this case, and μ is the linear absorption coefficient for silver [28]. A scattering factor is determined using Equation 2.6 [29].

$$f\left(\frac{sin\theta}{\lambda}\right) = \sum_{i=1}^{4} a_i exp\left(-b_i\left(\frac{sin\theta}{\lambda}\right)^2\right) + c \tag{2.6}$$

Where a_1=19.2808, a_2=16.6885, a_3=4.8045, a_4=1.0463, b_1=0.6446, b_2=7.4726, b_3=24.6605, b_4=99.8156 and c=5.179 [29]. A polarization factor is shown by Equation 2.7 [30]

$$f_p = \frac{\left(1+\cos^2\theta\right)}{2} \tag{2.7}$$

A Lorentz factor, which accounts for time each plane is exposed to x-rays for reflection, is represented by Equation 2.8 [31].

$$L \cong \frac{1}{\sin(2\theta)} \tag{2.8}$$

X-ray overspill accounts for loss in peak intensity when the x-ray beam is larger than the samples being analyzed [28] and is represented by Equation 2.9 [32].

$$f_x = \sin(\theta) \tag{2.9}$$

The values are corrected by incorporating each factor denoted previously and sample thickness into a single correction factor, shown by Equation 2.10,

$$F = (1 - f_a)\cdot f\left(\frac{\sin\theta}{\lambda}\right)\cdot f_p \cdot L \cdot f_x \tag{2.10}$$

and dividing the original value for the area under a peak in an x-ray diffraction pattern by that correction factor, as shown by Equation 2.11,

$$I_c = \frac{I_0}{F} \tag{2.11}$$

where F is the correction factor and I_0 is the original area under an intensity peak from an XRD spectrum.

2.4.3 Transmission Electron Microscopy

Transmission electron microscopy was utilized to analyze cross-sections of sample films because TEM has the resolution necessary to view microstructure details at the nanometer scale [33]. Elizabeth A. Ellis performed all TEM work for this project. Sections of film samples were removed using an FIB lift-out technique such that cross-sections of film samples could be analyzed. The removed sections were then thinned and examined using TEM.

The technique utilized to calculate the average nanotwin spacing for each film is illustrated in Figure 2.3. Average nanotwin spacing for representative thin film samples of high thickness (~1800 nm) was determined using Image J image analysis software. A cross-section of a film sample was analyzed using TEM; an example cross-section and grain boundaries of columnar grains are shown in Figure 2.3 (a). Ten different grains containing nanotwins are evaluated per sample cross-section. Figure 2.3 (b) demonstrates a close-up image of a single grain and nanotwins within that grain. The average of ten grains per sample was calculated by plotting a gray scale of a 100 nm length along a grain, orthogonal to the nanotwins; this is shown in Figure 2.3 (c) and (d). The gray scale spectrum, Figure 2.3 (d), indicates how light or dark a pixel is in a TEM image along that 100 nm line. Each peak in the spectrum represents a nanotwin and so the average is determined by dividing the length of the line (100 nm) by the number of peaks, shown in Equation 2.12.

$$S_{NT} = \frac{l}{N_p} \tag{2.12}$$

Where l is the length of the line (100 nm) and N_p is the number of peaks in the gray scale spectrum. Average grain size in the TEM samples was also determined using Image J image

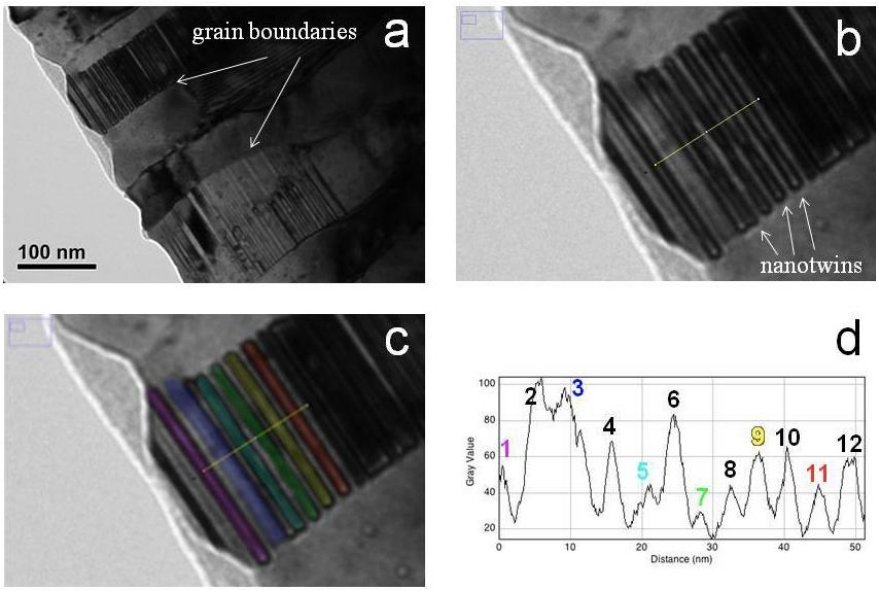

Figure 2.4: Demonstration of method used for calculating average nanotwin spacing in grains via TEM image analysis

analysis software and similar methodology to that used for estimating nanotwin spacing.

REFERENCES

[1] Smith DL. Thin-Film Deposition Principles and Practice. Boston, MA, U.S.A: McGraw-Hill, Inc.; 1995.

[2] Dahlgren SD. J Vac Sci Technol 1974;11:832.

[3] Zielinski EM, Vinci RP, Bravman JC. J Appl Phys 1994;76:4516.

[4] Greiser J, Muller D, Mullner P, Thompson C V, Arzt E. Scr Mater 1999;41:709.

[5] Greiser J, Mullner P, Arzt E. Acta Mater 2001;49:1041.

[6] Sonnweber-Ribic P, Gruber P, Dehm G, Arzt E. Acta Mater 2006;54:3863.

[7] Sonnweber-Ribic P, Gruber PA, Dehm G, Strunk HP, Arzt E. Acta Mater 2012;60:2397.

[8] Wang R, Dahlgren SD. J Mater Sci 1975;10:1456.

[9] Zhang X, Wang H, Chen XH, Lu L, Lu K, Hoagland RG, Misra A. Appl Phys Lett 2006;88.

[10] Hodge AM, Wang YM, Barbee Jr. TW. Mater Sci Eng A 2006;429:272.

[11] Anderoglu O, Misra a., Wang H, Zhang X. J Appl Phys 2008;103:094322.

[12] Velasco L, Polyakov MN, Hodge AM. Scr Mater 2014;83:33.

[13] Bufford D, Wang H, Zhang X. Acta Mater 2011;59:93.

[14] Furnish TA, Hodge AM. APL Mater 2014;2:046112.

[15] Zhang X, Misra a., Wang H, Nastasi M, Embury JD, Mitchell TE, Hoagland RG, Hirth JP. Appl Phys Lett 2004;84:1096.

[16] Zhang X, Misra A, Wang H, Shen TD, Nastasi M, Mitchell TE, Hirth JP, Hoagland RG, Embury JD. Acta Mater 2004;52:995.

[17] Bunshah RF. J Vac Sci Technol 1974;11:633.

[18] Ohring M. Materials Science of Thin Films: Deposition and Structure, Second. Academic Press; 2002.

[19] Reichelt W. Angew Chem Internat Ed 1975;14:218.

[20] Vossen JL, Kern W, editors. Thin Film Processes II. San Diego, CA, U.S.A.: Academic Press, Inc.; 1991.

[21] Vossen JL, Kern W, editors. Thin Film Processes. New York, NY, U.S.A.: Academic Press, Inc.; 1978.

[22] Szpunar J a., Ahlroos S, Tavernier P. J Mater Sci 1993;28:2366.

[23] Nagao K, Kagami E. Rigaku J 2011;27:6.

[24] Müller J, Balzar D, Geiss RH, Read DT, Keller RR. Comparison of Texture in Copper and Aluminum Thin Films Determined by XRD and EBSD, in:. Denver X-Ray Conf. Appl. X-Ray Anal. JCPDS-International Centre for Diffraction Data; 2006.

[25] Kužel R, Buršík J. Thin Solid Films 2013;530:2.

[26] Baker SP, Hoffman B, Timian L, Silvernail A, Ellis E a. Acta Mater 2013;61:7121.

[27] Baker SP, Saha K, Shu JB. Appl Phys Lett 2013;103:191905.

[28] Dinnebier RE, Friese K. Modern Xrd Methods in Mineralogy, accessed 10 Jun. 2015. URL: https://www.fkf.mpg.de/233448/xrd.pdf.

[29] Brown PJ, Fox AG, Maslen EN, O'Keefe MA, Willis BTM. Intensity of Diffracted Intensities, in:. Prince E (Ed.). Int. Tables Crystallogr., vol. C, third ed. Dordrecht, The Netherlands: Kluwer Academic Publishers; 2004.

[30] Warren BE. X-Ray Diffraction. Reading, MA, U.S.A.: Addison-Wesley Publishing Company, Inc.; 1969.

[31] Buerger MJ. Proc Natl Acad Sci U S A 1940;26:637.

[32] Hoffman B. Priv Conversat 2015.

[33] Williams DB, Carter CB. Transmission Electron Microscopy Basics I. New York, NY, U.S.A.: Plenum Press; 1996.

CHAPTER THREE

INFLUENCE OF NANOTWIN DENSITY ON TEXTURE TRANSFORMATION IN E-BEAM EVAPORATED SILVER THIN FILMS

Texture transformation has been previously theorized to be driving by minimization of surface and interface energies and strain energy [1–5]; however additional experimental evidence indicates that texture transformation occurs even when strain energy is not large enough to drive the transition [6–10]. Thin film defect density may serve as an additional driving force [6,8–10]. In this chapter nanotwin defects are investigated as a driving force for texture transformation in e-beam evaporated silver thin films.

3.1 Experimental Setup

3.1.1 Silver Film Deposition

Silver thin film samples were prepared following the procedures outlined in Chapter Two. A silicon wafer with an aluminum shield fixed across the center diameter of the wafer was mounted on a rotatable stage directly above an evaporation hearth. A linear shutter was positioned such that the edge of the linear shutter was parallel to the aluminum shield across the substrate and half of the substrate was shielded from evaporating source material. A sample shutter was positioned such that the substrate was shielded from evaporating source material. The vacuum chamber of the evaporator was pumped down and once a base pressure of ~ $2x10^{-6}$ Torr was reached deposition was started. First the titanium source material was heated with an electron beam and once a stable deposition rate of ~ 1 nm/s was obtained the sample shutter was rotated away from the substrate and a layer of titanium was deposited on the half of the substrate left exposed by the linear shutter. Once a layer of ~ 40-50 nm of titanium was achieved the sample shutter was rotated back towards the substrate to shield it from additional titanium adatoms and the electron beam was powered down.

Next the sample stage was rotated 90 ° such that the aluminum shield was orthogonal to the edge of the linear shutter. The motorized linear shutter was positioned such that the entire substrate was exposed. The silver source material was then heated with an electron beam and

once a desired stable deposition rate was obtained the sample shutter was rotated away from the substrate and deposition of a silver film was started. The motorized linear shutter was programmed such that the linear shutter would gradually cover the substrate resulting in a film with a thickness gradient. Film sample parameters (thickness and deposition rates) are listed in Table 3.1. Once film deposition was complete the vacuum chamber was vented and then the film was removed from the vacuum chamber for analysis. Film thicknesses were determined using contact profilometry.

3.1.2 Sample Annealing

After profilometry measurements were obtained, films were cleaved into ~ 5 mm by 5 mm square samples. Only samples with a titanium adhesion layer were utilized. Samples were taken along the diameter previously shielded by the aluminum shield such that sample thickness varied. Samples from films 1, 2, 6 and 8 were annealed following the first setup described in Chapter Two. The samples were placed on a hot plate with a thermocouple measuring surface temperature of the hot plate and a piece of aluminum foil tented over the hot plate to promote temperature uniformity. Samples were annealed in air for 2 hours at a temperature of 200 °C. Representative samples with a larger thickness (~ 1800 nm) were cleaved from deposited films. Samples from films 3, 5 and 7 were annealed via the second setup described in Chapter Two. An aluminum dish was placed in a hot oil bath such that it was partially submerged. Samples were placed in the aluminum dish with a thermocouple measuring surface temperature of the dish and an aluminum cover was placed over the dish to promote temperature uniformity. The samples

Table 3.1: Thickness and deposition rate details for silver thin film samples

Film	Thickness (nm)	Deposition Rate (nm/s)
1	490-1000	0.9
2	1075-1500	1.0
3	1800	1.1
4	1720	3.6
5	1820	4.4
6	480-1250	4.8
7	1830	11.2
8	300-1400	11.7

were annealed in air over time at a temperature of 100 °C.

3.1.3 Sample Analysis

X-ray diffraction measurements are obtained to determine (111) fractional intensity, an approximation for texture, of samples prior to and after heat treatment for the first setup and before, during and after annealing for the second annealing setup. Long range 2θ scans were obtained to determine what grain orientations for silver were present in film samples; the 2θ scan range was 35-80 ° except for the sample deposited at 3.6 nm/s which was analyzed using a 2θ scan range of 30-50 °. Localized scans were also obtained to minimize time samples were removed from heating sources for analysis during annealing; a 2θ scan range of 36.1-40.1 ° for (111) oriented grains and a 2θ scan range of 42.3-46.3 ° for (100) oriented grains.
Transmission electron microscopy images of sample cross-sections for as-deposited thicker samples from films 3, 4 and 7 were obtained. Samples were prepared for TEM analysis using FIB lift-out. Image analysis software was utilized to identify nanotwins in sample microstructure and was also used to measure average grain size and average nanotwin spacing for each sample.

3.2 Results

X-ray diffraction measurements were used to calculate (111) fractional intensity of as-deposited film samples prior to annealing, the results are shown in Figure 3.1. The (111) fractional intensity measurements shown in Figure 3.1 demonstrate that these silver film samples have strong (111) as-deposited texture. The results in Figure 3.1 also show that all silver film samples regardless of sample thickness or the rate at which a sample was deposited have strong (111) as-deposited texture.

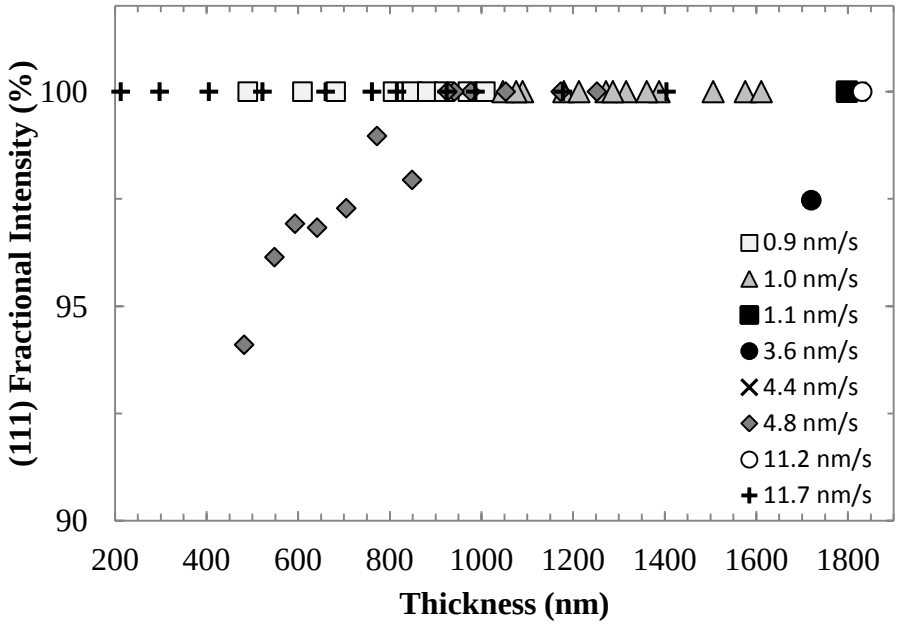

Figure 3.1: As-deposited (111) fractional intensity of silver thin film samples with varied thicknesses

Next, (111) fractional intensity values were calculated from x-ray diffraction measurements of silver film samples taken post heat treatment using the first annealing setup described previously, the results are presented in Figure 3.2. In Figure 3.2 the (111) fractional intensity of each film sample is shown as a function of sample thickness. The silver film samples came from films that were deposited using four different deposition rates. From Figure 3.2 it can be ascertained that film samples with larger thickness have lower (111) fractional intensity after heat treatment. Also the results in Figure 3.2 show that samples of similar thickness from silver films deposited at different deposition rates have different (111) fractional intensity values post-anneal; samples from films deposited at a faster deposition rate have lower (111) fraction intensity after annealing than samples of similar thickness from films deposited at a lower deposition rate. In addition, the (111) fractional intensity results presented in Figure 3.2 demonstrate that some of the silver film samples have mixed texture after heat treatment, so the samples only partially transformed when annealed.

From x-ray diffraction measurements taken periodically while representative samples with larger thickness (~1800 nm) were annealed using the second setup described previously

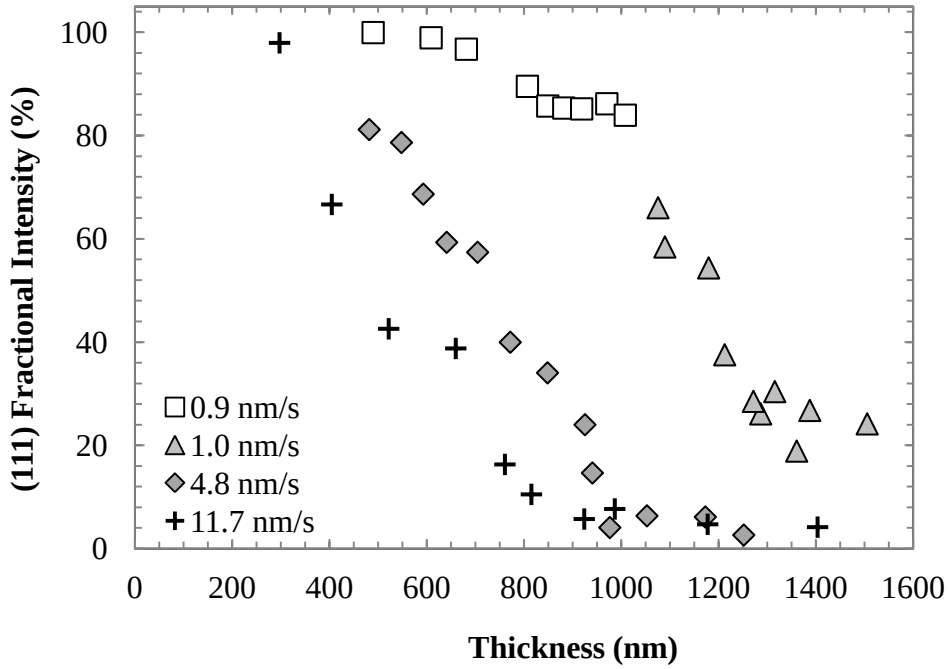

Figure 3.2: (111) fractional intensity of silver thin film samples with various thicknesses deposited at different rates then annealed at T = 200 °C in air for 2 h

(111) fractional intensity values were calculated and the results are shown in Figure 3.3. In Figure 3.3, the (111) fractional intensity of three samples deposited at different rates are presented as a function of time. From Figure 3.3 it is shown that the (111) fractional intensity of samples deposited at different rates changes in different amounts of time; samples from films deposited at a faster deposition rate take less time to fully transform than samples from films deposited at a slower deposition rate. The sample deposited at 1.1 nm/s was annealed for ~ 128 hours, the sample deposited at 4.4 nm/s was annealed for ~ 5 hours, and the sample deposited at 11.2 nm/s was annealed for ~ 1.8 hours. The annealing times do not account for time a sample was removed from heating source for XRD measurements. Also from Figure 3.3 it can be determined that the sample deposited at 1.1 nm/s only partially transformed with heat treatment.

For the sample silver film samples, TEM images of cross-sections from each sample are shown in Figure 3.4. Figure 3.4 (a) is a cross-section from a film sample deposited at 1.1 nm/s, the film sample shown in Figure 3.4 (b) was deposited at a rate of 3.6 nm/s and Figure 3.4 (c) is

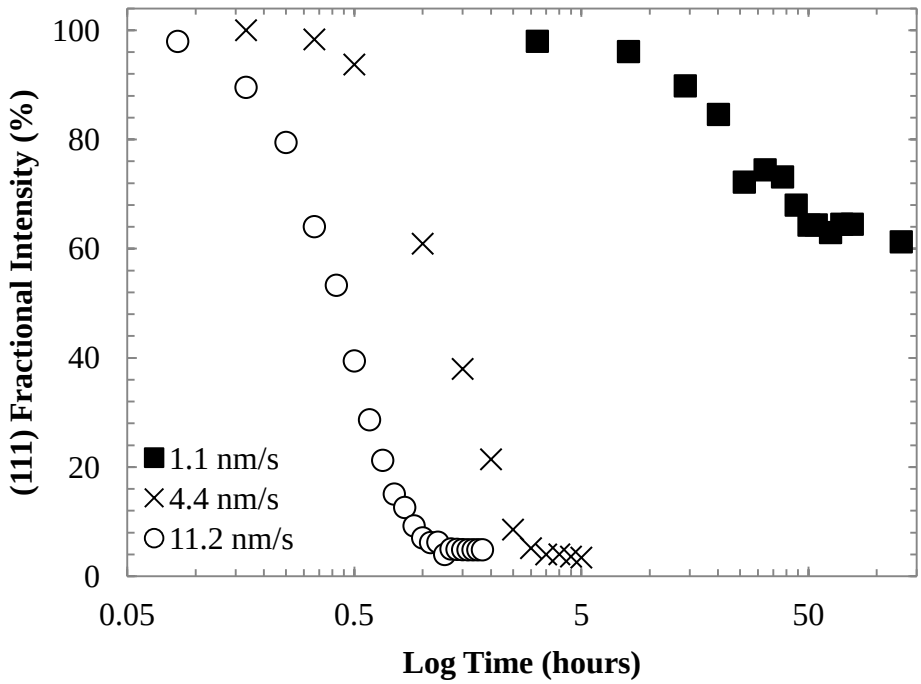

Figure 3.3: (111) fractional intensity of three silver thin film samples with identical thicknesses annealed at T = 100 °C in air demonstrating time dependence of texture transformation

of a sample deposited at 11.2 nm/s. The grains shown in these figures are columnar and contain nanotwins. Nanotwin spacing was determined for each film sample using the procedures described in Chapter 2. Nanotwin spacing for the sample shown in Figure 3.4 (a) is ~ 11 nm, for the sample shown in Figure 3.4 (b) is ~ 8 nm and for the sample shown in Figure 3.4 (c) is ~ 6 nm. From the nanotwin spacing results it can be ascertained that samples from silver films deposited at different rates have different nanotwin spacing; samples from films deposited at faster rates have smaller nanotwin spacing and since all films samples presented have a similar

Figure 3.4: TEM images of thin film sample cross-sections showing nanotwins in grains; deposition rates for samples presented are (a) 1.1 nm/s, (b) 3.6 nm/s and (c) 11.2 nm/s

thickness of ~ 1800 nm there are more nanotwins in a sample from a film deposited at a faster rate.

3.3 Discussion

From the experimental results it has been shown that nanotwins exist in silver thin films and that varying the rate at which a film was deposited directly affects the nanotwin density of that film. In addition it has been shown that texture transformation occurs in silver thin films and that the texture transformation is influenced by changes in deposition rate. And so it follows that nanotwins present in silver thin films play a role in texture transformation.

The (111) fractional intensity results presented as a function of film sample thickness in Figure 3.2 indicate that thinner samples retain a (111) texture while thicker films transform to (100) texture, as predicted by the earlier surface energy minimization and strain/interface energy minimization argument, but the results also indicate that samples of intermediate thicknesses transform partially and have mixed (111) and (100) texture. The samples which show a mixed texture after heat treatment do not follow the earlier argument which stated that films would either retain their as-deposited (111) texture or fully transform to (100) texture post anneal. These results support the idea that other driving forces in addition to surface energy minimization and strain/interface energy minimization must play a role in texture transformation of metal thin films.

Also, if texture transformation was only controlled by minimization of surface energy and strain/interface energy, as previously theorized [1–5] then only film thickness would play a role and the (111) fractional intensity results presented in Figure 3.3 would show essentially the same curve for all three samples, that had a similar thickness, rather than showing similar curves that shift to the right as deposition rate decreased. To better understand the change in rate of texture transformation energy from nanotwins in film sample microstructures was evaluated. Considering a film with entirely (111) as deposited texture that transforms completely to an entirely (100) texture that a specific thickness, h, the change in surface energy is governed by

Equation 1.3 and the energy from nanotwins, assuming all nanotwins are eliminated during heat treatment, is governed by Equation 3.1

$$\Delta\phi_t = N\gamma_t \tag{3.1}$$

where N is the number of nanotwins in a film sample and γ_t is the twin boundary energy of silver. If the energy obtained through elimination of nanotwins is greater than the energy cost of creating (100) surface then texture transformation will occur. In Equation 1.3 γ_{100} = 1.271 J/m^2 and γ_{111} = 1.087 J/m^2 [9–11]. In Equation 3.1 γ_t = 8 mJ/m^2 [12–14]. The changes in surface energy and nanotwin energy were calculated for each film sample; the results are presented in Figure 3.5. The energy available from nanotwins in the film samples increases with increasing deposition rate and so it follows that films deposited at a faster rate have a larger driving force for texture transformation and will therefore transform at a faster rate than films deposited at slower deposition rates.

Another important result from this work is the discovery of nanotwins in silver film samples that had been synthesized using electron-beam evaporation rather than a form of sputtering. Most reports on nanotwins in FCC metal thin films have been about film samples that

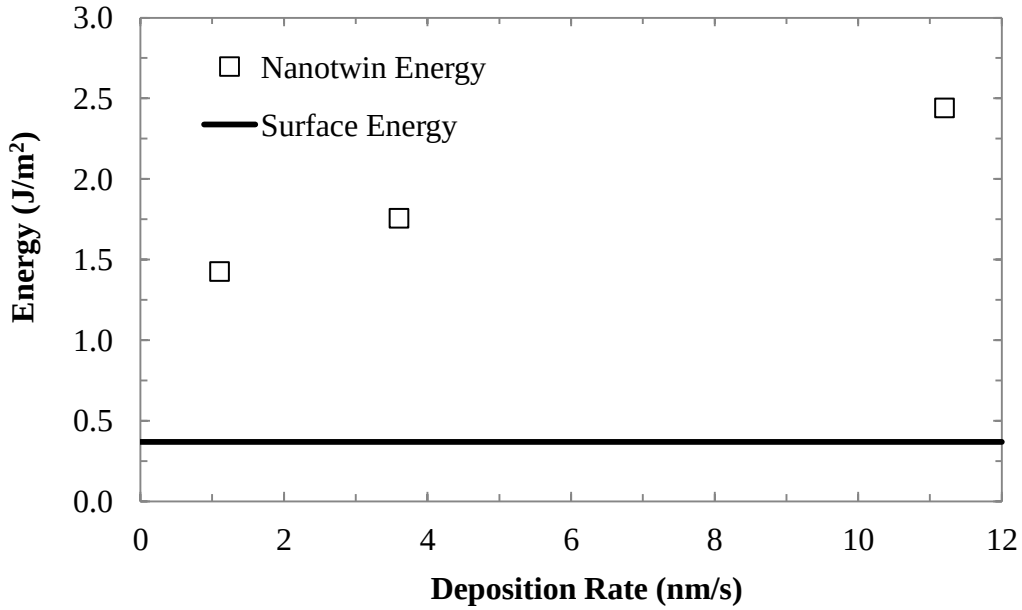

Figure 3.5: Comparison of energies for texture transformation in silver thin film samples deposited at three different deposition rates

were deposited using a form of sputtering [15–24]. A key difference between sputtering and evaporation deposition techniques is that sputtering involves transfer of kinetic energy while evaporation entails transfer of thermal energy [25]; because incoming atoms have a high kinetic energy during sputtering formation of defects in a film are more likely than for films synthesized using evaporation [26]. This work has shown that nanotwins are formed in thin films synthesized using evaporation, and not sputtering, so these defects may be a common occurrence in FCC metal thin films.

3.4 Conclusions

From the results of this work it has been shown that texture transformation occurs in silver thin films. The texture transformation has been shown to be influenced by varying sample thickness and the rate at which samples were deposited. The (111) fractional intensity of thicker samples is less than that of thinner samples and samples of the same thickness that were deposited at faster deposition rates had lower (111) fractional intensity values than samples deposited at slower deposition rates. From TEM results it has been shown that nanotwin defects exist in e-beam evaporated silver thin films. The nanotwins have been shown to be influenced by varying deposition rate. Nanotwin spacing was lower in samples deposited at faster deposition rates, thus samples deposited at faster rates have a larger nanotwin density. Because texture transformation increases in samples deposited at faster deposition rates and nanotwin density increases in samples deposited at faster deposition rates it follows that texture transformation is directly related to nanotwin density, samples with larger nanotwin density will have lower (111) fractional intensity values after heat treatment.

REFERENCES

[1] Zielinski EM, Vinci RP, Bravman JC. J Appl Phys 1994;76:4516.

[2] Floro JA, Thompson C V, Carel R, Bristowe PD. J Mater Res 1994;9:2411.

[3] Thompson CV, Carel R. Mater Sci Eng B 1995;32:211.

[4] Carel R, Thompson CV, Frost HJ. Acta Mater 1996;44:2479.

[5] Thompson CV, Carel R. Mater Sci Forum 1996;204-206:83.

[6] Greiser J, Muller D, Mullner P, Thompson C V, Arzt E. Scr Mater 1999;41:709.

[7] Greiser J, Mullner P, Arzt E. Acta Mater 2001;49:1041.

[8] Sonnweber-Ribic P, Gruber PA, Dehm G, Strunk HP, Arzt E. Acta Mater 2012;60:2397.

[9] Baker SP, Hoffman B, Timian L, Silvernail A, Ellis E a. Acta Mater 2013;61:7121.

[10] Baker SP, Saha K, Shu JB. Appl Phys Lett 2013;103:191905.

[11] Baskes MI. Phys Rev B 1992;46:2727.

[12] Rosengaard N, Skriver H. Phys Rev B 1993;47:12865.

[13] Humphreys FJ, Hatherly M. Recrystallization and Related Annealing. Oxford, UK: Elsevier Science Ltd.; 1995.

[14] Porter DA, Easterling KE, Sherif MY. Phase Transformations in Metals and Alloys, Third. Boca Raton, FL: CRC Press; 2009.

[15] Dahlgren SD. J Vac Sci Technol 1974;11:832.

[16] Wang R, Dahlgren SD. J Mater Sci 1975;10:1456.

[17] Zhang X, Wang H, Chen XH, Lu L, Lu K, Hoagland RG, Misra A. Appl Phys Lett 2006;88.

[18] Hodge AM, Wang YM, Barbee Jr. TW. Mater Sci Eng A 2006;429:272.

[19] Anderoglu O, Misra a., Wang H, Zhang X. J Appl Phys 2008;103:094322.

[20] Velasco L, Polyakov MN, Hodge AM. Scr Mater 2014;83:33.

[21] Bufford D, Wang H, Zhang X. Acta Mater 2011;59:93.

[22] Furnish TA, Hodge AM. APL Mater 2014;2:046112.

[23] Zhang X, Misra a., Wang H, Nastasi M, Embury JD, Mitchell TE, Hoagland RG, Hirth JP. Appl Phys Lett 2004;84:1096.

[24] Zhang X, Misra A, Wang H, Shen TD, Nastasi M, Mitchell TE, Hirth JP, Hoagland RG, Embury JD. Acta Mater 2004;52:995.

[25] Arunkumar P, Kuanr SK, Babu KS. Thin Film: Deposition, Growth Aspects, and Characterization, in:. Moorthy SBK (Ed.). Thin Film Struct. Energy Appl. Cham, Switzerland: Springer International Publishing; 2015.

[26] Anderoglu O. Nanoscale Growth Twins in Sputtered Copper Films. Texas A&M, 2010.

CHAPTER FOUR

INFLUENCE OF DEPOSITION RATE ON NANOTWIN DENSITY IN E-BEAM EVAPORATED SILVER THIN FILMS[1]

Shelby L. Johnson[1], Nathaniel G. Rogers[1], Elizabeth A. Ellis[1], Kyle Flemington[2], Paul Lashomb[2], Jonathon Yuly[2], Brandon Hoffman[2], and Shefford P. Baker[1*]

1. Cornell University, Department of Materials Science and Engineering, Bard Hall, Ithaca, NY 14853

2. Houghton College, Department of Physics and Earth Science, 1 Willard Avenue, Houghton, NY 14744

** Corresponding Author*

4.1 Abstract

Silver thin films were synthesized using electron beam evaporation. Deposition rate was varied during film synthesis. From transmission electron microscopy images of film sample cross-sections it was determined that deposition rate influence nanotwin formation in silver thin films. Increasing deposition rate correlated to decreased nanotwin spacing. A modified classical nucleation theory is applied and briefly reviewed. It was determined that a more suitable model probably exists for characterizing thin film microstructures.

4.2 Introduction

Planar defects, such as stacking faults and twin boundaries that are parallel to the substrate and orthogonal to the film growth direction, have been seen in various face-centered cubic (FCC) metal thin film microstructures including copper [1–11], nickel [12], stainless steel [13–15], gold [16], palladium [17,18], and silver [19–21] films. A portion of the copper films have been synthesized using electrodeposition [4,6,7,9,10]; however we are interested in physical vapor deposition (PVD) techniques. To date, sputtering is the primary PVD method used in reports of nanotwinned films [2,3,5,12–15,19–21].Very few studies [17,18] have

[1] This chapter is a research paper to be submitted to Acta Materialia

reported nanotwins in films produced by evaporation, another PVD method. In vapor-deposited films, a series of mostly coherent nanometer scale twin boundaries, or nanotwins, have been found to develop in (111) oriented grains as films are deposited [1,2,4,5,11–22]. The potential of nanotwins as a strengthening mechanism for metal thin films has regenerated interest in these defects; films containing nanotwins have been found to be harder than untwinned material [4–6,8,10,13,19,23,24]. Strengthening is proposed to result from nanotwins blocking dislocation motion [3–6,8,10,13,19,23].

Whether or not nanotwin density can be tailored by adjusting deposition parameters is of interest to determine the extent to which film strength can be tuned. This question is still debated. Zhou and Wadley [22] performed molecular dynamics simulations of copper film vapor deposition in a model where nanotwin formation was determined by a competition between growth of twinned and untwinned islands. Lateral growth was found to be so fast relative to reasonable deposition rates that identical simulated Cu microstructures were obtained when temperature and deposition rates were altered; thusly Zhou and Wadley [22] concluded that temperature and deposition rate had no significant effect on nanotwin formation [22]. In comparison, Zhang *et al.* [25] applied a model based on classical nucleation theory in solidification, as modified by Han *et al.* [26] to incorporate twin boundary formation, altered for deposition of a solid film from a vapor phase. This model predicts that nanotwin spacing should decrease with increasing deposition rate [25]. Indeed Zhang *et al.* [15] noted an increase in nanotwin density in their sputter-deposited 330 stainless steel films with increased deposition rate; however this was because the volume fraction of grains containing nanotwins increased with deposition rate, not because of a change in nanotwin spacing. In addition, Anderoglu *et al.* [8] found that the nanotwin spacing decreased with increasing deposition rate in sputtered copper thin films, while Zhang *et al.*[15] and Amin-Ahmadi *et al.*[17] found no effect of deposition rate on nanotwin spacing for sputtered Cu and e-beam evaporated Pd films, respectively.

Additional deposition parameters including temperature and stacking fault energy of source material have been found to have an influence on nanotwin development. Researchers have found that nanotwin spacing is correlated to deposition temperature; smaller nanotwin spacing results from using lower deposition temperatures [2,3]. Stacking fault energy has been found to influence nanotwin development, materials with lower stacking fault energies have been found to have greater nanotwin densities and smaller nanotwin spacing than films deposited from source materials with greater stacking fault energies [11,12,27]. Based on these experimental results deposition parameters do appear to influence nanotwin development in thin films.

In this paper, the influence of deposition rate on nanotwin density in electron beam evaporated thin films is investigated by depositing silver films to similar thicknesses under identical conditions with the exception of varying the rate at which each film is deposited. We find copious nanotwin boundaries in all films and a dependence of nanotwin spacing on deposition rate. We consider the rate dependence in terms of existing nucleation and growth models. Since the functionality and reliability of a film is strongly influenced by its microstructure [28–30], the existence of a relationship between deposition rate and nanotwin density provides a mechanism by which film defect densities and thusly film microstructures and material properties can be controlled and tailored for applications.

4.3 Experimental Setup

Samples were prepared using a method described in detail elsewhere [31]. Briefly, an adhesion layer of titanium was deposited onto a 100 mm Si substrate (native oxide only) followed by deposition of silver. For all films, the base pressure was ~ 2×10^{-6} Torr, Ti was evaporated from 99.995 % pure pellets in a graphite crucible and Ag was evaporated from 99.99 % pure pellets in a molybdenum crucible. To minimize contamination, a sample shutter that shaded the substrate from the source was closed while metal (Ti or Ag) deposition was initiated. The shutter was opened only after the deposition rate, as determined using a vibrating crystal monitor, had stabilized at a desired magnitude. Ti was deposited at a rate of ~ 10 nm/s to a thickness of 40-50 nm. For Ag, three different deposition rates were utilized for three different

samples: 1.1 nm/s, 3.6 nm/s, and 11.2 nm/s. During silver deposition, a thickness gradient was created using a computer-controlled motorized linear shutter, but we selected parts with a thickness near 1800 nm from each sample for the present study. Sample parameters are listed in Table 4.1. The temperature of the substrate was not controlled during deposition, but was measured using a thermocouple secured to the substrate.

Immediately following deposition, each substrate was removed from the vacuum chamber and film thickness was measured using a contact profilometer. The substrates were then cleaved into ~ 5 mm by 5 mm pieces with sides parallel and perpendicular to the Ag thickness gradient. While the thickness of each piece varied by about 50 nm in one dimension due to the gradient, each piece was assigned a single nominal Ag thickness value corresponding to the thickness at its center. When samples were not being measured or tested they were stored in a freezer to prevent grain growth from occurring at room temperature [32].

The texture of the Ag films on individual sample pieces was investigated using x-ray diffraction with Cu Kα radiation. The θ–2θ geometry was investigated to find what grain orientations were present in each sample.

Cross-section samples were prepared for transmission electron microscopy using the Focused Ion Beam (FIB) lift-out method. To protect the surface of the film samples from beam damage, the film samples were first capped with a layer of carbon and a layer of platinum. Two parallel trenches were then cut into the film using a Ga ion beam and a thin cross-section of the film was removed. For the FIB lift-out cuts, the ion beam was operated at a voltage of 30 kV and a current of 28 pA-6.5 nA. Final thinning was performed using ion beam parameters of 2-5 kV

Table 4.1: Silver films parameters of samples investigated in this paper including deposition rate at which each sample was deposited, film thickness, average grain size and average nanotwin spacing.

Deposition Rate (nm/s)	Thickness (nm)	Average Grain Size (nm)	Average Nanotwin Spacing (nm)
1.1	1798	130	11
3.6	1720	89	8
11.2	1831	75	6

and 28 pA normal to the surface of the film. Cross-section images of each sample were taken using transmission electron microscopy. A beam voltage of 120 kV was used when obtaining TEM images.

4.4 Results

The substrate temperature was found to not exceed 60 °C during deposition. The change in substrate temperature during the deposition process (~35 °C maximum) was determined to be inconsequential to the film microstructure.

4.4.1 Microstructure of As-Deposited Films

As in previous work [31,33], XRD of as-deposited films showed no significant Ag peaks other than those from (111)- and (100)-oriented grains. Thus, an estimate of relative amounts of the (111) and (100) texture components was obtained from the peak intensities using Equations 4.1 and 4.2. The {111} and {002} peak intensities were normalized individually using the scattering factor, absorption factor, and Lorentz polarization factor to obtain values that scale with the volume of the scattering material. We then approximated the volume fractions of the (111) and (100) texture components from the fractional intensities as

$$f_{111} = \frac{I_{111}}{I_{111} + I_{100}} \tag{4.1}$$

and

$$f_{100} = \frac{I_{100}}{I_{111} + I_{100}}\ , \tag{4.2}$$

where I_{111} and I_{100} are the corrected {111} and {002} integrated peak intensities, respectively. In the as-deposited state, the Ag film samples considered showed (111) fractional intensities near 100%, shown in Figure 4.1, indicative of strong (111) textures.

TEM images presented in Figure 4.2 show cross-sections of the as-deposited film samples. The silver films have columnar grain structures. Nanotwins are observed parallel to the substrate. The grain sizes and nanotwin densities were estimated from TEM pictures using image processing and analysis software. The average nanotwin spacing was found to be 11 nm, 8 nm

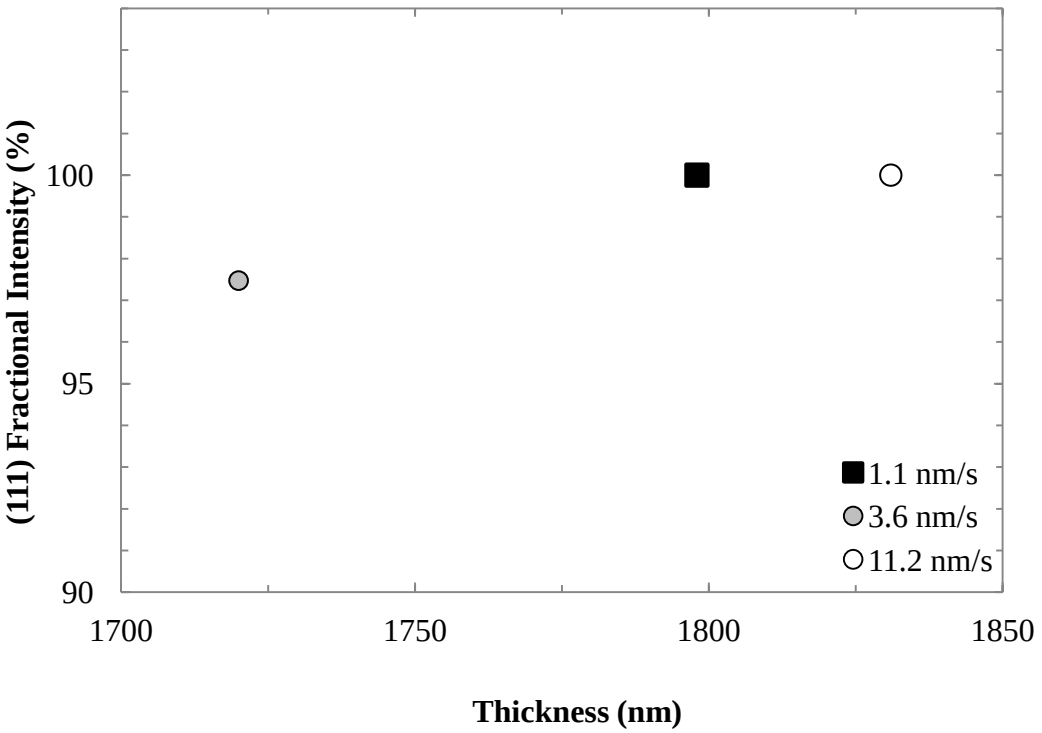

Figure 4.1: Results of XRD analysis showing (111) fractional intensity for silver thin films samples deposited at different deposition rates

and 6 nm for film samples deposited at 1.1 nm/s, 3.6 nm/s and 11.2 nm/s respectively. The average grain size was found to be 130 nm, 89 nm and 75 nm for film samples deposited at 1.1 nm/s, 3.6 nm/s and 11.2 nm/s respectively. Both the grain size and the nanotwin spacing decrease as deposition rate increases. The variation of nanotwin spacing with deposition rate is shown in Figure 4.3. The nanotwin spacing is cut in half for an order of magnitude increase in deposition rate.

4.5 Discussion

TEM images in Figure 4.2 and nanotwin spacing estimates listed in Table 4.1 are evidence that a direct correlation exists between deposition rate and nanotwin density in silver thin films. To understand this correlation, the mechanism by which nanotwins nucleate and grow during deposition must be understood.

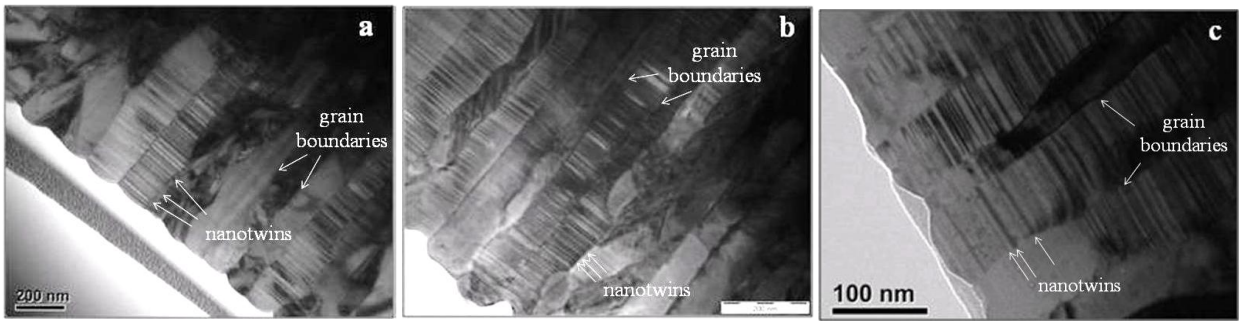

Figure 4.2: TEM images of sample cross-sections for silver film samples deposited at (a) 1.1 nm/s, (b) 3.6 nm/s, and (c) 11.2 nm/s. The grain size and the nanotwin spacing both decrease with increasing deposition rate (Table 4.1).

4.5.1 Nanotwin Formation

As in this work, nanotwins have been found in (111) oriented grains of FCC metal thin films [5,12,13,22]. The development of nanotwins in (111) grains during deposition has been attributed to the stacking sequence for the (111) orientation in FCC, which follows an ABCABC sequence [22]. The ABCABC stacking sequence enables incoming adatoms to occupy sites that either follow the sequence to form a perfect close-packed plane, continuing the ABCABC sequence, or that start the formation of a twin, resulting in a sequence such as ABCBCA [1,22,26].

The mechanism by which nanotwins grow during deposition is not yet fully understood. A proposed mechanism exists for films synthesized utilizing pulsed electrodeposition which attributes the formation of nanotwins to relaxation of strain built up during deposition [4][9]. Pulsed electrodeposition consists of a short "on time" during which fast deposition takes place, followed by a longer "off time" during which deposition does not occur [4]. Strain develops during the brief "on time" when deposition rate is fast and this strain is relieved by the development of nanotwins during the longer "off time" when recrystalization and grain growth occur [4][9]. This proposed mechanism does not apply to techniques like sputtering and evaporation because deposition is continuous with these methods. Another key difference is that nanotwins are observed in plan view TEM images parallel to each other on a grain surface,

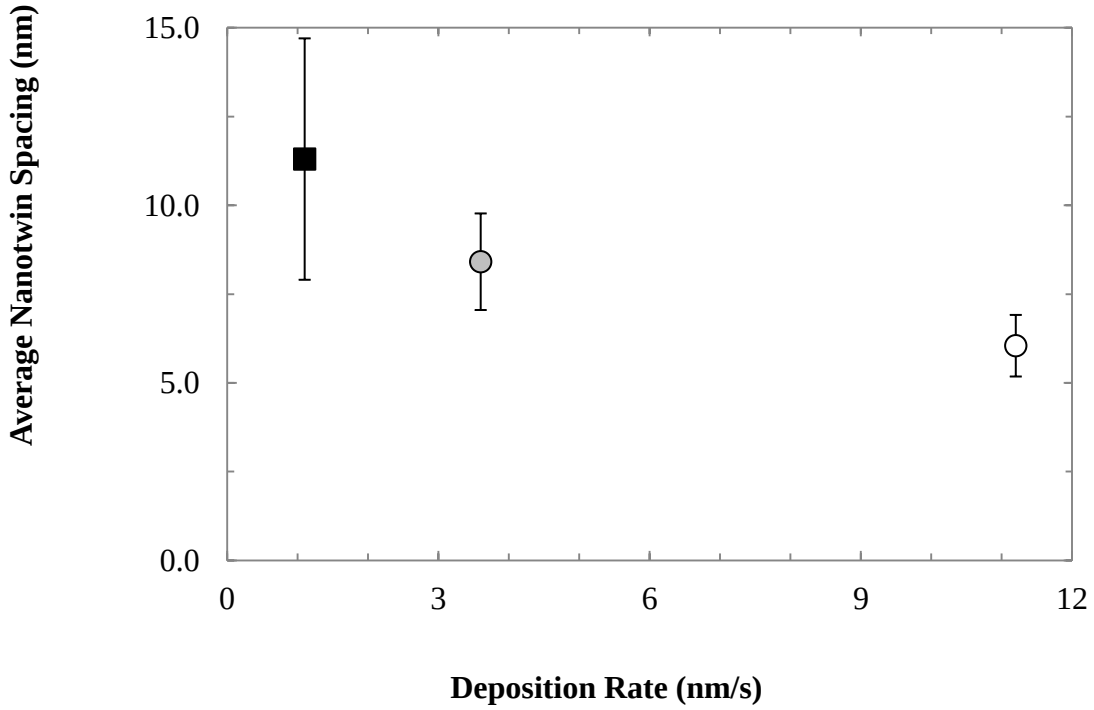

Figure 4.3: Measured nanotwin spacings as a function of growth rate in e-beam evaporated silver thin films.

whereas the nanotwins of interest for this work are observed in cross-section view TEM images parallel to each other in layers with the growth direction of a film.

For films made using physical vapor deposition techniques such as sputtering and evaporation, Zhou and Wadley [22] investigated this problem using atomistic modeling (molecular dynamics and statics calculations) to determine a twin growth mechanism and associated energy parameters during vapor deposition and combined these results with a phase field analysis to simulate the development of a twin domain during deposition. Zhou and Wadley [22] modeled vapor deposition of copper thin films in different crystallographic orientations and found that nanotwins only occurred for simulations in the (111) growth direction. Additional results revealed that the probability of twin formation was dependent on the initial distribution of nuclei and that twin domains grow laterally quickly [22]. Zhou and Wadley [22] also varied deposition rate and temperature parameters and concluded that because

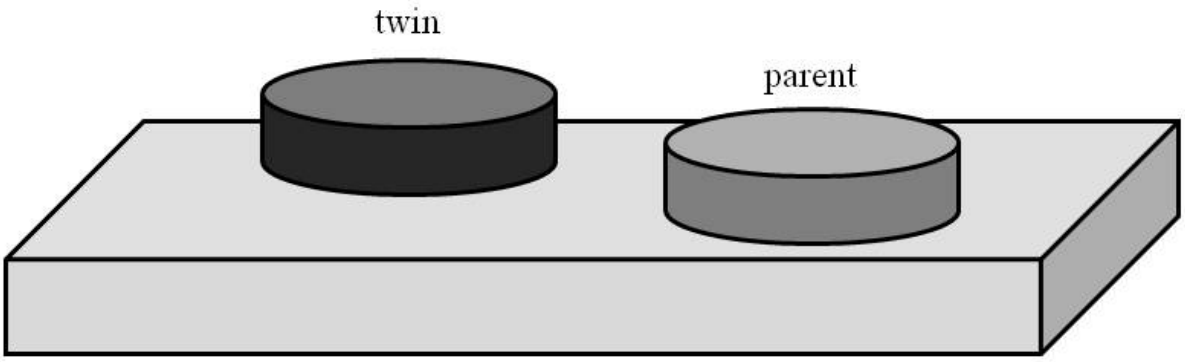

Figure 4.4: Illustration of discs growing on substrate demonstrating classical nucleation theory

the lateral growth of the domains is so fast deposition parameters do not significantly influence the development of nanotwins in thin films.

An alternative analysis introduced by Zhang *et al.* [25] is the use of capillary theory for homogeneous nucleation from a vapor phase to understand nanotwin development during film growth, demonstrated in Figure 4.4. Zhang *et al.* [25] sputter deposited copper and 330 stainless steel multilayer films and adapted a model for homogeneous nucleation from Han *et al.* [26], for nucleation of twin and non-twin domains in the shape of discs as a result of undercooling, to explain their experimental observations regarding nanotwins in 330 stainless steel and copper multilayer film samples. This analysis predicts that parameters like deposition rate and stacking fault energy influence nanotwin formation in thin films. Using the model applied by Zhang *et al.* [25] nanotwin spacing can be estimated using Equations 4.3 - 4.5.

$$J = \frac{P_V}{\sqrt{2\pi mkT}} \tag{4.3}$$

$$\Delta G_V = \frac{kT}{\Omega}\ln\left(\frac{P_V}{P_S}\right) \tag{4.4}$$

$$\ln\left(\frac{I_{perfect}}{I_{twin}}\right) = \frac{\pi\gamma^2 h\gamma_t}{kt\Delta G_v\left(h\Delta G_v - \gamma_t\right)} \tag{4.5}$$

In Equation 4.3 J is the flux of depositing atoms, P_v is the pressure of the supersaturated vapor, m is the atomic mass of the depositing species, k is the Boltzmann constant, and T is the substrate temperature in Kelvin; in Equation 4.4 Ω is the atomic volume and P_s is the vapor pressure above

the solid; in Equation 4.5 $I_{perfect}$ is the nucleation rate of perfect domains, I_{twin} is the twin domain nucleation rate, γ is the surface energy of the depositing material, γ_t is the twin boundary energy of the depositing material, and h is the interatomic spacing between (111) planes [25]. Applying this model to our data $J = 1.52\text{x}10^{15}$, $4.98\text{x}10^{15}$, and $1.55\text{x}10^{16}$ monolayers/s for the respective deposition rates of 1.1, 3.6, and 11.2 nm/s; T = 300 K; $\Omega = 1.71\text{x}10^{-29}$ m^3/atom [34]; γ = 1.087 J/m^2 [35]; γ_t = 8 mJ/m^2 [36–39], h = 7.076 m [34]; and $P_s = 2\text{x}10^{-6}$ Torr. P_s is estimated by measuring the background pressure of the vacuum chamber prior to deposition [40]. Results from applying this model to our deposition parameters are predicted nanotwin spacing values of 23 nm, 8 nm, and 4 nm for films deposited at 1.1 nm/s, 3.6 nm/s, and 11.2 nm/s respectively. We found that the proposed model does agree with our experimental nanotwin spacing measurements of 11 nm, 8 nm, and 6 nm for films deposited at 1.1 nm/s, 3.6 nm/s, and 11.2 nm/s respectively and follows the predicted trend of decreasing nanotwin spacing with increased deposition rate, but the predicted nanotwin spacing values are not an exact match to our experimental measurements.

4.5.2 Analysis of Nucleation Model

A source of error is the γ_t parameters. The value for γ_t has been reported to be 8 mJ/m^2 [36][37][39]. These values are approximations and variations of this parameter also significantly impacts results produced by Equation 4.5. Although the twin boundary energy for silver has often been reported to be 8 mJ/m^2 [36–39] a range of values from 8-19 mJ/m^2 [36][38,41]. Without knowing which result is most accurate, selecting a value for the twin boundary energy parameter remains a source of error. A sensitivity analysis of the twin boundary energy parameter for calculating nanotwin spacing is shown in Figure 4.5. Also, rather than using surface energy to approximate the additional energy associated with growth of nuclei, an alternative would be to include the step energy associated with growth of a nucleus on a surface since atoms are being incorporated into a growing nucleus at a step and so the area of this step grows with the domain.

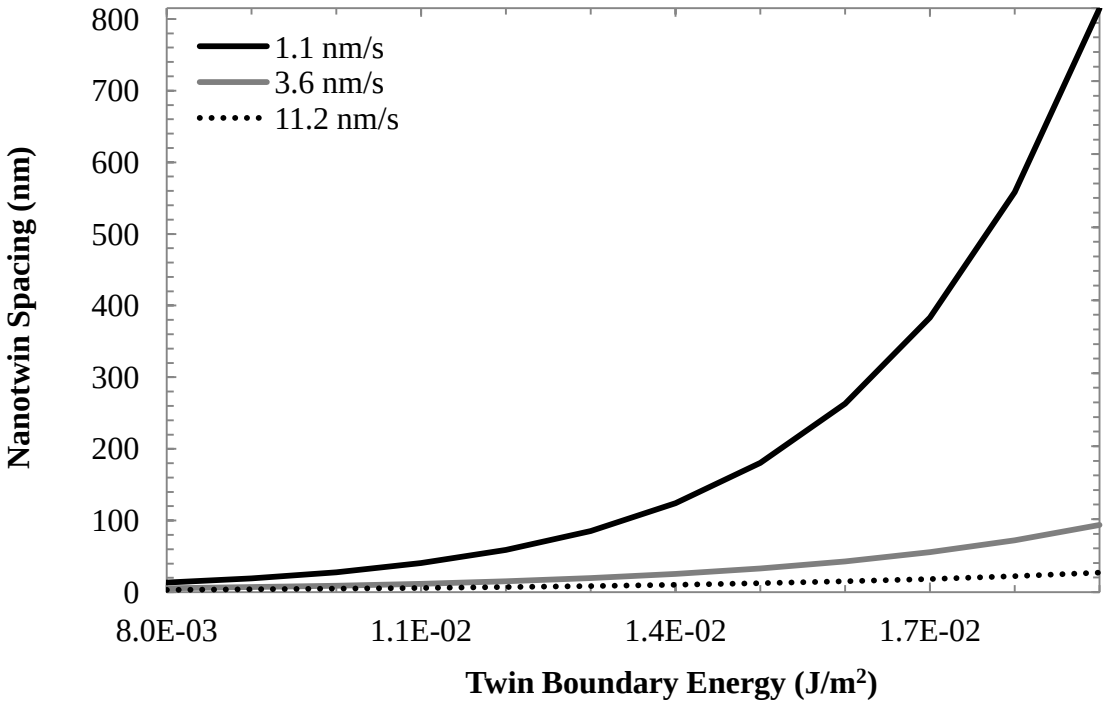

Figure 4.5: Sensitivity analysis of model predicting nanotwin spacing with regard to twin boundary energy parameter

An additional potential source of error in this model is the parameter P_s. A sensitivity analysis of the P_s parameter for calculating nanotwin spacing is shown in Figure 4.6.Velasco *et al.* [11] also made use of the model applied by Zhang *et al.* [25] and noted discrepancies between calculated and experimentally observed nanotwin spacing when applying the model to their Cu-Al alloy thin films. Velasco *et al.* [11] also list P_s as a source for this error. Altering P_s has significant impact on model results and thus knowing the appropriate value is extremely important.

On another note, the use of classical nucleation theory to describe thin film deposition may not be suitable. In classical nucleation theory P_s represents the equilibrium vapor pressure of the source material at substrate temperature [42][43][44][45], which for silver was determined to be 1.17×10^{-40} Torr at a substrate temperature of 300 K using Equation 4.6 [46].

$$\log(P) = 2.881 + A + BT^{-1} + C\log(T) + DT^{-3} \quad (6)$$

In Equation (4.6) P is in Torr, T is in Kelvin, A=9.127, B=-14999, C=-0.7845 for solid silver [46]. When this value for P_s is used and the traditional classical nucleation theory is followed the

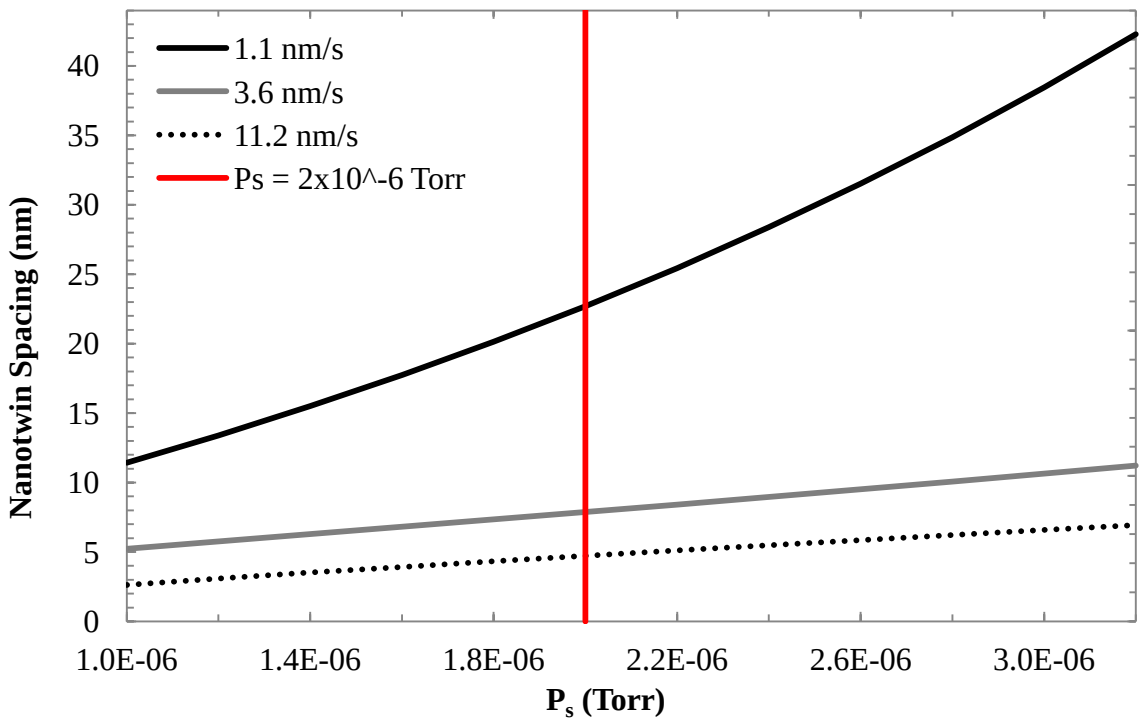

Figure 4.6: Sensitivity analysis of model predicting nanotwin spacing with regard to Ps parameter

results are significantly different than experimental measurements, although the same trend of decreased nanotwin spacing with increased deposition rate is followed. The predicted nanotwin spacing results are 0.7198 nm, 0.7194 nm and 0.7191 nm for film samples deposited at 1.1 nm/s, 3.6 nm/s and 11.2 nm/s respectively. These results indicate that the nanotwin spacing does not change significantly when deposition rate is varied, which is not in agreement with the experimental results posted in Table 4.1. The use of classical nucleation theory to describe how thin film microstructures develop during physical vapor deposition may not be appropriate. One thing to consider is that for the process used in this work to synthesize the thin film samples, e-beam evaporation, the system is far from equilibrium [47] which supports the concept that classical nucleation theory is not suitable for analysis. This conclusion was also reached by Cinti [43] and Thompson and Carel [44] in earlier work. In both research papers the authors conclude that the classical nucleation theory was not applicable [43] nor meaningful [44] for their respective analysis of films deposited from a vapor. The value that Zhang *et al.* [25] has

assigned to P_s for his analysis does not make sense as the background pressure of the vacuum chamber prior to film deposition is not influenced by the depositing material, it is the pressure of remaining trace gasses in the chamber after the chamber has been pumped down [45]. Further investigation of this theory and alternative nucleation models is necessary.

4.5.3. Nanotwin Spacing and Deposition Rate

Results from the present work are unique in that the nanotwin spacing of the silver film samples analyzed in this paper changed with deposition rate. Variations in nanotwin spacing with deposition rate have been reported elsewhere: Velasco *et al.* [11] report an increase in nanotwin spacing as deposition rate is increased and, in contrast, Anderoglu *et al.* [8] report a decrease in nanotwin spacing as deposition rate is increased, as we found in our work. However, most research on nanotwins in thin films in which deposition rate was varied found that no changes in nanotwin spacing occur [15][17]. The results from this work support that changing deposition rate influences nanotwin development in thin films by decreasing nanotwin spacing in thin films such that defect density is increased. Additional research may be necessary to demonstrate this trend in other FCC metal thin films.

4.6 Summary and Conclusions

Results from analysis of silver thin film samples deposited using three different deposition rates via e-beam evaporation show that nanotwin formation is directly influenced by deposition rate. As the deposition rate used to synthesize the silver films was increased, the spacing of the nanotwins in the samples decreased, resulting in larger defect densities.

To better understand the relationship between deposition rate and nanotwin spacing a nucleation model was investigated. The nucleation model applied by Zhang *et al.* [25] was found to closely estimate nanotwin spacing for silver thin films based on the experimental parameters of the present work; however, the relevancy of this modified classical nucleation theory to physical vapor deposition is still questionable. Further research into alternative nucleation models is necessary.

4.7 Acknowledgments

This work was supported by the National Science Foundation (NSF) via grant Nr. DMR-1106223 and DMR-1411024, including a Research Experiences for Undergraduates supplement. This work made use of the Cornell Center for Materials Research Shared Facilities which are supported through the NSF MRSEC program (DMR-1120296). Brandon Hoffman, Kyle Flemington, Paul Lashomb and Jonathon Yuly received additional financial support from Houghton College.

REFERENCES

[1] Vook RW, Witt F. J Vac Sci Technol 1965;2:49.

[2] Dahlgren SD. J Vac Sci Technol 1974;11:832.

[3] Merz MD, Dahlgren SD. J Appl Phys 1975;46:3235.

[4] Lu L, Shen Y, Chen X, Qian L, Lu K. Science (80-) 2004;304:422.

[5] Zhang X, Wang H, Chen XH, Lu L, Lu K, Hoagland RG, Misra A. Appl Phys Lett 2006;88.

[6] Cui BZ, Han K, Xin Y, Waryoba DR, Mbaruku a. L. Acta Mater 2007;55:4429.

[7] Zhang X, Tu KN, Chen Z, Tan YK, Wong CC, Mhaisalkar SG, Li XM, Tung CH, Cheng CK. J Nanosci Nanotechnol 2008;8:2568.

[8] Anderoglu O, Misra a., Wang H, Ronning F, Hundley MF, Zhang X. Appl Phys Lett 2008;93:1.

[9] Xu D, Sriram V, Ozolins V, Yang JM, Tu KN, Stafford GR, Beauchamp C. J Appl Phys 2009;105.

[10] Lu L, Chen X, Huang X, Lu K. Science (80-) 2009;323:607.

[11] Velasco L, Polyakov MN, Hodge AM. Scr Mater 2014;83:33.

[12] Wang R, Dahlgren SD. J Mater Sci 1975;10:1456.

[13] Zhang X, Misra a., Wang H, Nastasi M, Embury JD, Mitchell TE, Hoagland RG, Hirth JP. Appl Phys Lett 2004;84:1096.

[14] Zhang X, Misra a., Wang H, Swadener JG, Lima a. L, Hundley MF, Hoagland RG. Appl Phys Lett 2005;87:1.

[15] Zhang X, Anderoglu O, Misra a., Wang H. Appl Phys Lett 2007;90:153101.

[16] Vook RW, Witt F. J Vac Sci Technol 1965;2:243.

[17] Amin-Ahmadi B, Idrissi H, Galceran M, Colla MS, Raskin JP, Pardoen T, Godet S, Schryvers D. Thin Solid Films 2013;539:145.

[18] Idrissi H, Amin-Ahmadi B, Wang B, Schryvers D. Phys Status Solidi Basic Res 2014;251:1111.

[19] Bufford D, Wang H, Zhang X. Acta Mater 2011;59:93.

[20] Bufford D, Wang H, Zhang X. J Mater Res 2013;28:1729.

[21] Furnish TA, Hodge AM. APL Mater 2014;2:046112.

[22] Zhou XW, Wadley HNG. Acta Mater 1999;47:1063.

[23] Zhang X, Misra a., Wang H, Lima a. L, Hundley MF, Hoagland RG. J Appl Phys 2005;97.

[24] Hodge AM, Wang YM, Barbee Jr. TW. Mater Sci Eng A 2006;429:272.

[25] Zhang X, Misra A, Wang H, Shen TD, Nastasi M, Mitchell TE, Hirth JP, Hoagland RG, Embury JD. Acta Mater 2004;52:995.

[26] Han K, Hirth JP, Embury JD. Acta Mater 2001;49:1537.

[27] Dahlgren SD, Nicholson WL, Merz MD, Bollmann W, Devlin JF, Wang R. Thin Solid Films 1977;40:345.

[28] Vinci RP, Zielinski EM, Bravman JC. Thin Solid Films 1995;262:142.

[29] Hommel M, Kraft O. Acta Mater 2001;49:3935.

[30] Sonnweber-Ribic P, Gruber PA, Dehm G, Strunk HP, Arzt E. Acta Mater 2012;60:2397.

[31] Baker SP, Hoffman B, Timian L, Silvernail A, Ellis E a. Acta Mater 2013;61:7121.

[32] Ellis EA, Chmielus M, Lin M-T, Joress H, Visser K, Woll A, Vinci RP, Brown WL, Baker SP. Submitt to Acta Mater 2015.

[33] Baker SP, Saha K, Shu JB. Appl Phys Lett 2013;103:191905.

[34] Gray T. Technical Data for Silver, accessed 17 Jul. 2015.
URL: http://periodictable.com/Elements/047/data.html.

[35] Baskes MI. Phys Rev B 1992;46:2727.

[36] Rosengaard N, Skriver H. Phys Rev B 1993;47:12865.

[37] Humphreys FJ, Hatherly M. Recrystallization and Related Annealing. Oxford, UK: Elsevier Science Ltd.; 1995.

[38] Bernstein N, Tadmor E. Phys Rev B 2004;69:094116.

[39] Porter DA, Easterling KE, Sherif MY. Phase Transformations in Metals and Alloys, Third. Boca Raton, FL: CRC Press; 2009.

[40] Zhang X. Priv Conversat 2015.

[41] Kibey S, Liu JB, Johnson DD, Sehitoglu H. Acta Mater 2007;55:6843.

[42] Pound GM, Simnad MT, Yang L. J Chem Phys 1954;22:1215.

[43] Cinti RC, Chakraverty BK. Surf Sci 1972;30:125.

[44] Thompson CV, Carel R. Mater Sci Eng B 1995;32:211.

[45] Ohring M. Materials Science of Thin Films: Deposition and Structure, Second. Academic Press; 2002.

[46] Alcock CB. Vapor Pressure of the Metallic Elements-Equations, in:. Haynes WM, Bruno TJ, Lide DR (Eds.). CRC Handb. Chem. Phys., 95th ed. CRC Press; 2014.

[47] Eckertova L. Physics of Thin Films. New York, NY, U.S.A.: Plenum Press; 1977.

CHAPTER FIVE

SUMMARY AND FUTURE WORK

5.1 Nanotwins and Texture Transformation

From our work analyzing texture transformation in silver thin films with varied nanotwin defect densities we showed that parallel planar defect density acts as an additional driving force for texture transformation. Film samples with higher nanotwin densities transformed at lower thicknesses than film samples with lower nanotwin densities under identical annealing conditions. Film samples with higher nanotwin densities also transform in less time than film samples of the same thickness with lower nanotwin densities under identical annealing conditions.

5.2 Deposition Rate and Nanotwin Formation

From our work investigating nanotwin densities in silver thin films deposited at different rates via electron beam evaporation we demonstrated that deposition rate directly affects nanotwin formation in thin films. Thin film samples deposited at faster rates contained a larger nanotwin density and the nanotwin spacing was smaller than film samples deposited at slower rates. These results are unique from previous work done by Zhang et al. [1] and Amin-Ahmadi [2] in which both researchers observed an increase in volume percent of grains containing nanotwins but did not observe a change in nanotwin spacing when deposition rate was changed. This has implications for making tunable thin film microstructures obtainable.

We also found that the nanotwin formation model proposed by Zhang et al [3] does effectively predict nanotwin spacing based on experimental parameters, but that some improvements can be made and that an alternative model may exist that is more appropriate for describing physical vapor deposition.

5.3 Future Work

Important questions still remain unanswered after this project. One topic that is debatable is whether or not nanotwins in thin films are stable. A method to study the stability of nanotwins in silver thin films would be to perform TEM in situ during annealing and record the grain

growth and changes to nanotwins in sample film microstructures. Another consideration if nanotwins are found to be unstable in thin films is to determine if grain boundaries and nanotwins could be pinned such that the microstructure does not vary significantly when heated. Nanotwin responses to deformation should also be investigated to determine nanotwin stability.

Many studies have recently evaluated nanotwins as a strengthening mechanism for thin films. Since we have demonstrated that nanotwin density can be controlled by changing deposition rate, the hardness of film samples with different nanotwin densities should be investigated via nanoindentation.

It would also be useful to evaluation if the trends observed in this work translate to other FCC metal and alloy films since very few other researchers have reported a change in nanotwin spacing with deposition parameters. These experiments would also serve to investigate the influence of stacking fault energy and twin formation energy on nanotwin formation in films.

Film samples with mixed texture post heat treatment have been observed in this work and in previous work [4]. Understanding why this occurs would shed more light on the mechanism and driving forces behind texture transformation and potentially lead to methods of controlling this phenomenon. Evaluating stresses that develop in film samples with different nanotwin densities via curvature measurements in situ during annealing would be a useful step in calculating if the additional energy from eliminating nanotwins makes up for the minimum stress required for complete transformation to occur.

Researchers have demonstrated the influence of substrate temperature on nanotwin density in thin films [5]. Substrate temperature directly influences atom mobility on a substrate during deposition and also influences the kinetics of film nucleation and growth. Higher substrate temperatures are expected to result in larger critical radii of nuclei for films. Additional research in this area and application of the classical nucleation model used in Chapter 4 would be useful for gaining further understanding of nanotwins in FCC metal thin films and also a way of evaluating the robustness of the classical nucleation theory based model for predicting thin film defect densities based on deposition parameters.

One final area that is still unclear is whether or not film microstructure can be predicted using a model. The classical nucleation theory model applied in this work has been questioned by other researchers [6][7] and may not be appropriate for physical vapor deposition. Additional models should be investigated to determine if a model exists that can accurately predict thin films microstructures, more specifically nanotwin formation, based on experimental parameters to optimize film production without performing multiple experimental trials.

REFERENCES

[1] Zhang X, Anderoglu O, Misra a., Wang H. Appl Phys Lett 2007;90:153101.

[2] Amin-Ahmadi B, Idrissi H, Galceran M, Colla MS, Raskin JP, Pardoen T, Godet S, Schryvers D. Thin Solid Films 2013;539:145.

[3] Zhang X, Misra A, Wang H, Shen TD, Nastasi M, Mitchell TE, Hirth JP, Hoagland RG, Embury JD. Acta Mater 2004;52:995.

[4] Baker SP, Hoffman B, Timian L, Silvernail A, Ellis E a. Acta Mater 2013;61:7121.

[5] Furnish TA, Hodge AM. APL Mater 2014;2:046112.

[6] Cinti RC, Chakraverty BK. Surf Sci 1972;30:125.

[7] Thompson CV, Carel R. Mater Sci Eng B 1995;32:211.